M. Grader, P. Gerlinger, Influence of operating conditions on flow field dynamics and soot formation in an aero-engine model combustor, Combust. Flame 258 (2023) 112712.

The original publication is available at www.elsevier.com

http://dx.doi.org/10.1016/j.combustflame.2023.112712

© <2023>. This manuscript version is made available under the CC-BY-NC-ND 4.0 license http://creativecommons.org/licenses/by-nc-nd/4.0/

Influence of operating conditions on flow field dynamics and soot formation in an aero-engine model combustor

Martin Grader[a,*], Peter Gerlinger[a]

[a] *DLR – German Aerospace Center, Pfaffenwaldring, 38-40, 70659 Stuttgart, Germany*

Abstract

Large-eddy simulations of a sooting aero-engine model combustor are performed for three operating points. They are analyzed to investigate the influence of secondary air injection and primary equivalence ratio on soot formation dynamics. It will be shown how the causes of a strongly intermittent sooting behavior can be investigated quantitatively by mode analysis and correlated statistics. Simulations rely on Arrhenius reaction rate-based finite-rate chemistry, where 79 species transport equations are solved simultaneously to accurately predict the combustion of ethylene: 43 species represent the gas phase, 36 the soot and soot precursors. Soot evolution is described by a well validated sectional soot model including a sectional model for polycyclic aromatic hydrocarbons and their radicals. This approach captures the influence of changing operating conditions on soot formation well. Hence, soot prediction is found to be accurate enough to investigate the formation processes. The presence of coherent and incoherent flow field dynamics in the combustor necessitates the use of multiresolution proper orthogonal decomposition and correlated statistics for the analysis. While the precessing vortex core is found to support soot production continuously, low frequency dynamics are identified to cause the intermittence at all operating conditions. Secondary air injection significantly increases the intensity of the low frequency dynamics. Yet, the soot volume in the combustor varies by the same order of magnitude without secondary air injection. The soot formation intermittence is closely linked to an axially symmetric mixture fraction mode near the primary injector at all operating conditions. Low mode energy required an additional mode analysis of joint statistics which confirmed this conclusion. Increasing the equivalence ratio at the primary injector decreases the influence of the low frequency dynamics on soot formation.

Keywords: Soot, Large-Eddy Simulation, Aero-Engine Model Combustor, Multiresolution POD, Soot Dynamics, Sectional Approach

*Corresponding author

Email address: martin.grader@dlr.de (Martin Grader)

1. Introduction

Aero-engine generated soot particles are known to adversely affect human health [1]. They also support contrail formation [2] which is the largest contributor to aviation caused global warming [3]. Reducing soot emissions of aero-engines requires a detailed understanding of the soot evolution process in the combustor. To facilitate scientific investigations of soot evolution under relevant conditions, an aero-engine model combustor (AEMC) [4] has been designed. It includes many features of an aero-engine combustor like swirled injection and secondary air injection. Strong soot intermittence has been observed both experimentally and in large-eddy simulations (LES) of this combustor [5, 6]. Low frequency dynamics (LFD) in the flow field have been identified to cause the intermittence [7]. The precessing-vortex core (PVC) influences soot evolution as well [8, 9]. It remained unclear whether these dynamics are affected by changing operating conditions. However, changing operating conditions strongly affect the mean sooting behavior of the combustor [4, 10]. Hence, this work extends previous studies by investigating the influence of the secondary air injection and the equivalence ratio of the primary injection on the flow field dynamics and the soot formation. Based on the detailed information provided by the LES, interactions of these dynamics can be analyzed in order to achieve a better understanding of how certain combustor features affect soot.

The studied sooting aero-engine model combustor has been extensively investigated experimentally [4, 5, 9, 11–14] and is part of the ISF turbulent flame database [15]. Thanks to the large validation database, many numerical studies of this test case have been conducted for model validation [8, 16–27] or to analyze the sooting behavior [6, 7, 10, 28]. LES was found to be necessary to properly simulate soot in this combustor [26]. The complex combustion process with premixed and non-premixed combustion regimes [5], a strong influence of differential-diffusion [20], large heat losses at the walls [13, 22], and recirculation of hot, burned gas necessitate the use of finite-rate chemistry (FRC) in this work. Feasibility of LES-FRC simulations of the AEMC has already been demonstrated [7, 18, 25, 26]. A wide variety of soot models has been applied in simulations of this combustor. Two-equation soot models (e.g., [8]), method-of-moment based models (e.g., [28]) and particle size distribution resolving models such as a Lagrangian approach (e.g., [21]) or a sectional approach (e.g., [25]) are found in literature. None of the simulations was able to completely reproduce the measured soot field in terms of distribution and magnitude. Yet, soot models with polycyclic aromatic hydrocarbons (PAH) based soot inception worked best in capturing the maxi-

mum soot volume fraction [17]. Therefore, a well validated sectional PAH model including reversible PAH growth [29] is used in this work together with a sectional soot model [30]. Its ability to reproduce the particle size distribution is especially useful for modeling surface dependent reactions. Expensive LES-FRC simulations require well validated models since parameter studies are hardly feasible. Validation of the current modelling approach has been done both for laminar [29, 30] and turbulent flames [25, 30, 31]. It is applied in the current work without any adjustments of the model constants.

Coherent and incoherent dynamics in the combustor as well as different temporarily separated but spatially overlapping soot evolution phenomena require appropriate analyzing methods. In this work, the former are treated by mode analysis while for the latter correlated statistics are utilized. The suitability of correlated statistics in analyzing the interdependency of variables in sooting flames have been demonstrated experimentally (e.g., [32, 33]) and in LES (e.g., [31, 34]). Mode analysis of sooting flames is hardly carried out since only few experiments exist that involve combustion dynamics. Furthermore, the large variety of timescales occurring in soot formation and convection necessitates appropriate mode analysis methods. Coherent flow field-, acetone- and OH- dynamics have been studied in the AEMC by means of phase averaging and proper orthogonal decomposition [14] (POD). Phase averaging requires long sampling times which are usually beyond current LES capabilities. POD needs less sampling time and facilitates interpretation by conserving all modes and ranking them by their importance. A drawback of POD is, that the energy-based mode decomposition can result in one mode consisting of several dynamics with different frequencies [35]. Previous application of POD to a sooting flame showed this behavior for soot volume fraction modes which makes an interpretation unambiguous [7]. Pure frequency-based methods like dynamic mode decomposition [36] can overcome this issue [35]. However, they are not well suited to analyze intermittent dynamics such as the soot evolution [35]. Several POD extensions (e.g., [37–39]) exist to improve the aforementioned POD deficiencies. Also, other mode analysis methods such as cluster-based reduced order modeling methods [40, 41] or machine learning algorithms [42] may be useful in the context of soot evolution. For a comprehensive review on POD strengths and weaknesses as well as alternative mode analysis methods the reader is referred to Taira et al. [35, 43]. Since multiresolution POD [37] (MRPOD) has been shown to work well for soot evolution mode analysis with LES data [7], it is applied in this work. It combines POD with wavelet-based frequency isolation to separate dynamics with similar energy but different frequencies. In this way, MRPOD meets all demands in order to analyze the intermittent soot formation,

while maintaining the advantage of mode energy ranking. In addition, it requires only a minimum of user input. Usually, mode analysis is performed for variables in physical space. This work will show, that mode analysis of the dynamics of statistics in temperature - equivalence ratio space provides useful additional information to interpret the influence of operating conditions on the soot dynamics.

2. Modeling and numerical method

2.1. Filtered transport equations

Unsteady filtered transport equations for mass, momentum and enthalpy conservation are solved in the LES framework. The FRC approach requires additionally to solve the filtered species transport equations

$$\frac{\partial \overline{\rho}\widetilde{Y}_\beta}{\partial t} + \frac{\partial \overline{\rho}\widetilde{u}_i\widetilde{Y}_\beta}{\partial x_i} - \frac{\partial}{\partial x_i}\left[\left(\overline{\rho}D_\beta + \frac{\mu_t}{Sc_t}\right)\frac{\partial \widetilde{Y}_\beta}{\partial x_i}\right] = \bar{\omega}_\beta \tag{1}$$

for the mass fraction Y of each chemical species β. Einstein notation and the filtered Reynolds ($\bar{\cdot}$) and Favre ($\tilde{\cdot}$) averages are applied. The velocity component u_i in x_i-direction, the density ρ, the molecular diffusion coefficient of each species D_β and the chemical source term ω_β are required to solve the set of equations. Arrhenius type reaction rates are used to calculated the chemical source term. D_β is calculated incorporating differential diffusion which is necessary to accurately predict soot in turbulent flames [20, 44–46]. Since molecular diffusion of soot is negligible [47] and thermophoretic transport is weak in turbulent flames [48], only diffusive transport of gas phase species is considered. Turbulence-chemistry interaction is modeled by a presumed-PDF approach [49, 50] assuming statistical independence of temperature, species and soot fluctuations. Sub-grid variance is calculated by a scale similarity approach [51, 52] frequently found in LES [53, 54]. The shape of the temperature PDF is assumed to be clipped Gaussian, the species PDF is a multivariate beta-PDF [49, 55] and a double-delta PDF is used for soot [56]. Flow field variables are calculated assuming an incompressible fluid. The influence of sub grid scale turbulent motion on the flow field is determined by the WALE model [57]. Heat radiation by an optically thin gas is considered [30].

2.2. Soot model

Michelsen et al. [58] recently defined a common soot evolution terminology, which is adopted in this work. Soot precursors and combustion chemistry are described by a well validated gas phase mechanism consisting of 43 species and 304 reactions [29]. It is a reduced version of the Slavinskaya and Frank [59] mechanism which was validated for the pyrolysis and combustion of short-chained hydrocarbons [60]. The reduced mechanism proofed its ability for combustion prediction in ethylene flames [7, 8, 26, 29, 31, 61–63].

A sectional model for polycyclic aromatic hydrocarbons [61, 64], which was improved and validated by Eberle et al. [29], is used to lump PAH and PAH radicals, respectively. It includes

reversible PAH chemistry and has been successfully applied in laminar and turbulent flame calculations [7, 30, 31, 63]. Three sections describe stable and radical PAHs, respectively, in a molar mass range between 100 and 800 g/mol, which is discretized logarithmically. Sub mechanisms for gas-phase interaction, growth by hydrogen-abstraction acetylene-addition (HACA) [65], growth by collisions between stable and radical PAHs and oxidation as well as PAH radical activation and deactivation are included. Soot particle inception is modeled by PAH-collision reactions involving the largest PAH or PAH radical section.

The soot section containing incipient soot particles is directly adjacent to the largest PAH section. This ensures mass conservation and a realistic incipient soot particle diameter of 1.28 nm is achieved assuming a soot density of 1800 g/mol [66]. The first soot section covers particles from 800 g/mol to 1600 g/mol and the subsequent 29 sections are scaled by a factor of two, respectively. Blacha et al. [61] developed the model and significant improvements were made by Eberle et al. [30] by adding soot aggregates to the modeling approach. These aggregates are formed beyond a critical diameter of 14 nm and grow both in primary particle size and number with increasing section number. Particle growth by coagulation, PAH deposition and the HACA mechanism are included in the model as well as oxidation by oxygen and the hydroxyl radical. An iterative procedure [61], used to calculate stoichiometric coefficients [67] of these reactions, maintains mass and atom conservation. The model and its validation are thoroughly described in literature [30, 61]. It has been successfully applied in turbulent flame calculations [30, 31, 61] without adjusting the model constants.

2.3. Numerical solver

The incompressible, unstructured, finite volume DLR in-house code ThetaCOM [64, 68] is used to perform all simulations. Transport equations are discretized by second order schemes in space and time. Pressure-velocity coupling is achieved by a projection method [69] and 84 transport equations are solved in total. The 79 transport equations describing the thermochemical state are solved fully coupled. Thus, interactions between e.g. gas phase and soot are captured consistently, conserving mass and atoms.

3. Analysis methods

Non-uniform computational grids, as required in this work, cover a wide range of cell volumes. Hence, both correlated statistics and energy-based mode analyses should take the cell volumes v_i into account. Therefore, a normalized cell volume

$$v_i^* = \frac{v_i M}{V}, \tag{2}$$

is introduced, where M is the number of cells in the analyzed computational domain V.

3.1. Correlated statistics

Normalized, two-dimensional joint histograms are used in this work to analyze filtered correlated statistical data. They are obtained by dividing the whole state space $s(\alpha_1, \alpha_2)$ of two variables α_1 and α_2 into $N_{\alpha_1} \cdot N_{\alpha_2}$ sections $k(\alpha_1, \alpha_2)$ with $N_{\alpha_1} = N_{\alpha_2} = 50$. The normalized frequency F_t^* of each section k is defined as

$$\mathrm{F}_t^*(k,t) = \frac{\sum_{i=1}^{M} v_i^* D_{i,t}|_{k(\alpha_1,\alpha_2)}}{\sum_{j=1}^{N_{\alpha_1}\cdot N_{\alpha_2}} \sum_{i=1}^{M} v_i^* D_{i,t}|_{j(\alpha_1,\alpha_2)}} \tag{3}$$

for one solution timestep t and for the whole simulation run as

$$\mathrm{F}^*(k) = \frac{\sum_{t=1}^{N}\sum_{i=1}^{M} v_i^* D_{i,t}|_{k(\alpha_1,\alpha_2)}}{\sum_{t=1}^{N}\sum_{j=1}^{N_{\alpha_1}\cdot N_{\alpha_2}} \sum_{i=1}^{M} v_i^* D_{i,t}|_{j(\alpha_1,\alpha_2)}}, \tag{4}$$

where N is the number of analyzed, equidistant timesteps. The occurrence of a statistical event conditioned on a section k reads

$$D_{i,t}|_{k(\alpha_1,\alpha_2)} = \begin{cases} 1, & \widetilde{\alpha}_1^{low(k)} < \widetilde{\alpha}_{1_{i,t}} \leq \widetilde{\alpha}_1^{up(k)} \cap \widetilde{\alpha}_2^{low(k)} < \widetilde{\alpha}_{2_{i,t}} \leq \widetilde{\alpha}_2^{up(k)} \\ 0, & \text{otherwise.} \end{cases} \tag{5}$$

The subscripts $low(k)$ and $up(k)$ denote the lower and upper limit of $k(\alpha_1, \alpha_2)$.

3.2. Multiresolution POD

The MRPOD methodology is based on snapshot POD [70] where a snapshot refers to the variable field at one timestep. Relevant differences are mentioned below and the reader is referred to Yin and Stöhr [37] for a detailed description of MRPOD. Two different LES data-sets are analyzed with MRPOD. The first consists of fluctuations of a filtered variable $\alpha'(x,t) = \widetilde{\alpha}(x,t) - \langle\widetilde{\alpha}(x)\rangle$ defined in space and time, which are rearranged in a matrix $\mathbf{A}(\alpha') \in \mathbb{R}^{N\times M}$ ($\langle\cdot\rangle$ denotes the temporal average). The second consists of fluctuations of correlated statistics $F_t'^*(k,t) = F_t^*(k,t) - \langle F_t^*(k)\rangle$

defined in time and the state space sections k which are rearranged in a matrix $\mathbf{B}(F_t'^*) \in \mathbb{R}^{N \times N_{\alpha_1} \cdot N_{\alpha_2}}$. Since the MRPOD procedure is identical for both data-sets, except that no volume weighting is necessary for the latter case, the MRPOD methodology is described for the data-set $\mathbf{A}$, only. If not mentioned by a corresponding subscript in the variable name, mode analysis is conducted for the whole computational domain.

Essentially, POD is a transformation of $\mathbf{A}$ based on the eigenvalues and orthogonal eigenvectors of the covariance matrix

$$\mathbf{K}(\alpha') = \mathbf{A}\mathbf{V}\mathbf{A}^T. \tag{6}$$

In case of constant density and $\alpha' = u'$, the main diagonal of $\mathbf{K}$ reflects the kinetic energy contained in each snapshot and trace($\mathbf{K}$) the kinetic energy of all snapshots. The term energy is used in the following, irrespective of α'. To maintain the correct energy content on non-uniform grids, the diagonal matrix $\mathbf{V} \in \mathbb{R}^{M \times M}$ is introduced [35]. It consists of the normalized cell volume v_i^* as diagonal elements in case of matrix $\mathbf{A}$ and is an identity matrix for $\mathbf{B}$. MRPOD requires $\mathbf{K}$ to be filtered using a two-dimensional maximum-overlap discrete wavelet packet transform (MODWPT), before proceeding with the snapshot POD procedure. In this work, the bandpass filters are constructed by Daubechies least asymmetric wavelet [71] with 20 basic elements and a decomposition level of 4. The subscript f of the filtered covariance matrix $\mathbf{K}_f(\alpha')$ is replaced in the analysis section by the actual name of the band-pass filter. Solving the eigenvalue problem

$$\mathbf{K}_f\mathbf{\Psi} = \mathbf{\Psi}\mathbf{\Lambda}, \tag{7}$$

results in the diagonal matrix $\mathbf{\Lambda}$ containing the eigenvalues $\lambda_{l,f}$ and the matrix $\mathbf{\Psi}$ containing the eigenvectors $\Psi_{l,f}$. Each pair of eigenvalue and eigenvector belongs to a mode l. They are used to construct the vector of temporal coefficients

$$a_{l,f}(\alpha') = \sqrt{\lambda_{l,f}}\Psi_{l,f}. \tag{8}$$

According to singular value decomposition, the vector of orthogonal spatial modes

$$\phi^\star_{l,f}(\alpha') = \frac{1}{\sqrt{\lambda_{l,f}}}\Psi_{l,f}\mathbf{A}\mathbf{V}^{\frac{1}{2}} \tag{9}$$

can be constructed. Yet, analysis of non-volume weighted reconstructed modes $\phi_{l,f} = \phi^\star_{l,f}\mathbf{V}^{-\frac{1}{2}}$ is advantageous, which are analyzed instead. The quantitative influence of certain modes (e.g. mode

one and two) of a variable α' at a specific position x and time step t can be assessed by reconstruction of the scalar

$$\alpha'_{1-2,f}(x,t) = \sum_{l=1}^{2} a_{l,f}(t,\alpha')\phi_{l,f}(x,\alpha'). \tag{10}$$

The influence of these modes on the mean field is given by

$$\widetilde{\alpha}_{1-2,f}(x,t) = \langle\widetilde{\alpha}(x)\rangle + \alpha'_{1-2,f}(x,t). \tag{11}$$

Summation over all filters and all modes results in complete reconstruction of the instantaneous variable field. The energy-based mode decomposition of POD and MRPOD makes the eigenvalue of a mode l indicating its energy content. Modes are ordered such that eigenvalues are decreasing with increasing mode number, which facilitates the identification of important modes. The normalized energy content

$$E^*_{l,f}(\alpha') = \frac{\lambda_{l,f}}{\mathrm{trace}(\mathbf{K})} \tag{12}$$

quantifies the relative importance of each MRPOD mode in comparison to all modes in the analyzed domain.

Coherent and incoherent dynamics require different methods to investigate interaction between modes of different field variables. Reconstructed coherent dynamics, like the PVC (in this work always $\alpha'_{1-2,PVC}$ with Eq. 10), often show a sinusoidal temporal evolution. For each variable and each point in the domain, a vector $\tau(x,\alpha'_{1-2,PVC}) = \left[t_0^1, t_0^2, ..., t_0^N\right]$ which contains the zero-crossing times from negative to positive can be defined. To minimize the influence of MODWPT boundary conditions on the reconstructed data, a time series of $15 < t < 285$ ms is investigated in this work. The local mean phase shift of two variables α' and γ'

$$\Delta\tau(x,\alpha',\gamma') = \langle\tau(x,\alpha'_{1-2,PVC}) - \tau(x,\gamma'_{1-2,PVC})\rangle \cdot f_{PVC} \cdot 360^\circ \tag{13}$$

is calculated by means of zero-crossing vectors arranged such that $t_0^1(x,\alpha'_{1-2,PVC}) < t_0^1(x,\gamma'_{1-2,PVC})$. For incoherent modes, like most LFD modes, the cross-correlation

$$R_{i,j}(\Delta t,\alpha',\gamma') = \langle a_{i,LFD}(t,\alpha')\ a_{j,LFD}(t+\Delta t,\gamma')\rangle \tag{14}$$

reveals the similarity of the temporal behavior of two variables. The normalized cross-correlation $R^*_{i,j}(\Delta t,\alpha',\gamma')$, normalized by the maximum of all cross-correlations of α' and γ', allows to rank their relative importance. For the normalization procedure, cross-correlations within $-50 < \Delta t < 50$ ms are considered to exclude irrelevant correlations.

4. Simulation Details

Figure 1 presents a schematic of the AEMC. Ethylene is concentrically injected through the primary injector into the shear layer of two swirled air flows. The injection of secondary air aims to mimic the rich-quench-lean (RQL) concept of industrial aero-engine combustors. An inner recirculation zone (IRZ) and an outer recirculation zone (ORZ) are present in the flow field. The main flow is separated from the IRZ and the ORZ by an inner and outer shear layer (ISL, OSL). The flow field has a V-shape close to the injector which propagates downstream via the periphery of the combustion chamber.

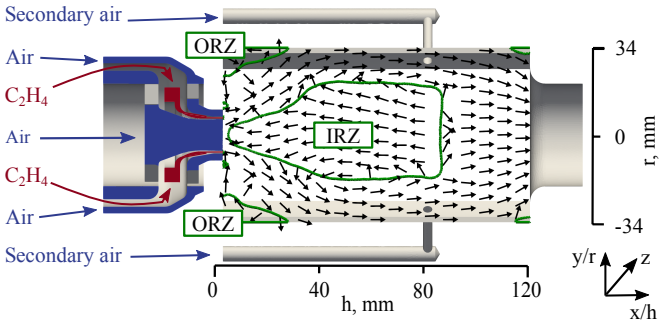

Figure 1: Schematic of the aero-engine model combustor. Green iso-contours of $\langle \widetilde{u}_x \rangle = 0$ m/s indicate recirculation, arrows the velocity field.

Table 1 summarizes the operating conditions which differ between each investigated operating point (OP). Equivalence ratio (ER) of the reference operating point [4], called OP-1, is fuel-rich at the primary injector ($ER_p = 1.2$) and becomes globally lean ($ER_g = 0.86$) by secondary air injection dilution. An increased fuel mass flow ($\dot{m}_{C_2H_4}$) at OP-2 increases both ER_p and ER_g compared to OP-1. Deactivating the secondary air injection ($\dot{m}_{air_2}$) at OP-3 only raises ER_g. Thereby the influence of the primary equivalence ratio and the secondary air injection on soot evolution can be assessed. The pressure at each operating point is three bar. Non-reacting (NR) operating conditions of OP-1 and OP-3 are considered as well (the data of OP-1 has already been used for validation [26]).

For a detailed description of the boundary conditions and the computational grid, the reader is referred to the supplementary material. Measured heat flux through the combustor windows [13] is set as thermal boundary condition. The computational grid used for all three simulations consists of about 7 million nodes and is locally refined at the primary injector and the secondary air injection. Statistics are sampled at 4000 Hz over 300 ms physical time. Each LES requires about 3.3 million

OP	ER_{p}	ER_{g}	$\dot{\mathrm{m}}_{\mathrm{C_2H_4}}$ [g/s]	$\dot{\mathrm{m}}_{\mathrm{air_2}}$ [g/s]
OP-1	1.2	0.86	0.82	4.04
OP-2	1.4	1.0	0.96	4.04
OP-3	1.2	1.2	0.82	0.00

Table 1: Differing operating conditions of the studied operating points.

CPUh on 1536 “Intel Xeon Platinum 8168” CPUs.

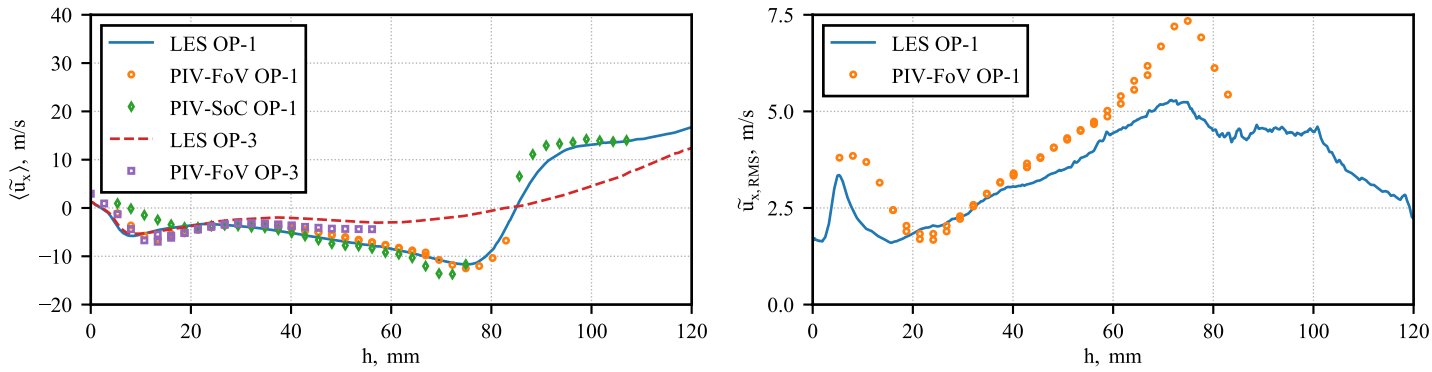

Figure 2: Experimental [12] (PIV) and simulated (LES) axial velocity component on the axis for OP-1 and OP-3. Left: Mean, right: RMS.

5. Validation

5.1. Flow field

Figure 2 compares the axial velocity on the axis of the AEMC. Two different "particle image velocimetry" (PIV) techniques were used to investigate the flow field in the AEMC: PIV-"field of view" (FoV) and PIV-"sum of correlation" (SoC). While PIV-FoV is restricted to a smaller measurement area as the PIV-SoC, it is more accurate. Moreover, RMS values can only be measured by means of PIV-FoV. For a more detailed discussion on PIV measurement techniques, the reader is referred to the literature (e.g. [12]). Differences between the results of the two PIV techniques and in the overlap area of PIV-FoV illustrate the measurement uncertainties. Taking the complex flow field into account, the agreement between simulation and experiment is good for both OP-1 and OP-3. Significant differences are found only in the RMS field close to the secondary air injection.

Figure 3 compares radial profiles of the axial velocity at four characteristic positions: One near the injector ($h = 3$ mm), one in the zone of primary combustion ($h = 18$ mm), one between the primary injector and the secondary air injection ($h = 45$ mm) and one close to the secondary air injection ($h = 80$ mm). The general agreement between experiment and simulation is very good, but some differences exist. Close to the injector, at the outer parts of the V-shaped profile ($-10 > r > 10$ mm), both measured mean and RMS axial velocity exceed the LES predictions. Further downstream, at $h = 18$ mm, this behavior persists. At $h = 45$ mm the profiles agree much better, while the LES slightly underestimates the recirculation velocity for both OPs. Close to the secondary air injection, at $h = 80$ mm, mean values of simulation and measurement of OP-1 agree well within the measurement uncertainties. No measurement data is available for OP-3. Similar to the axial profiles, the RMS in the center of the combustor is underestimated by the LES. This also

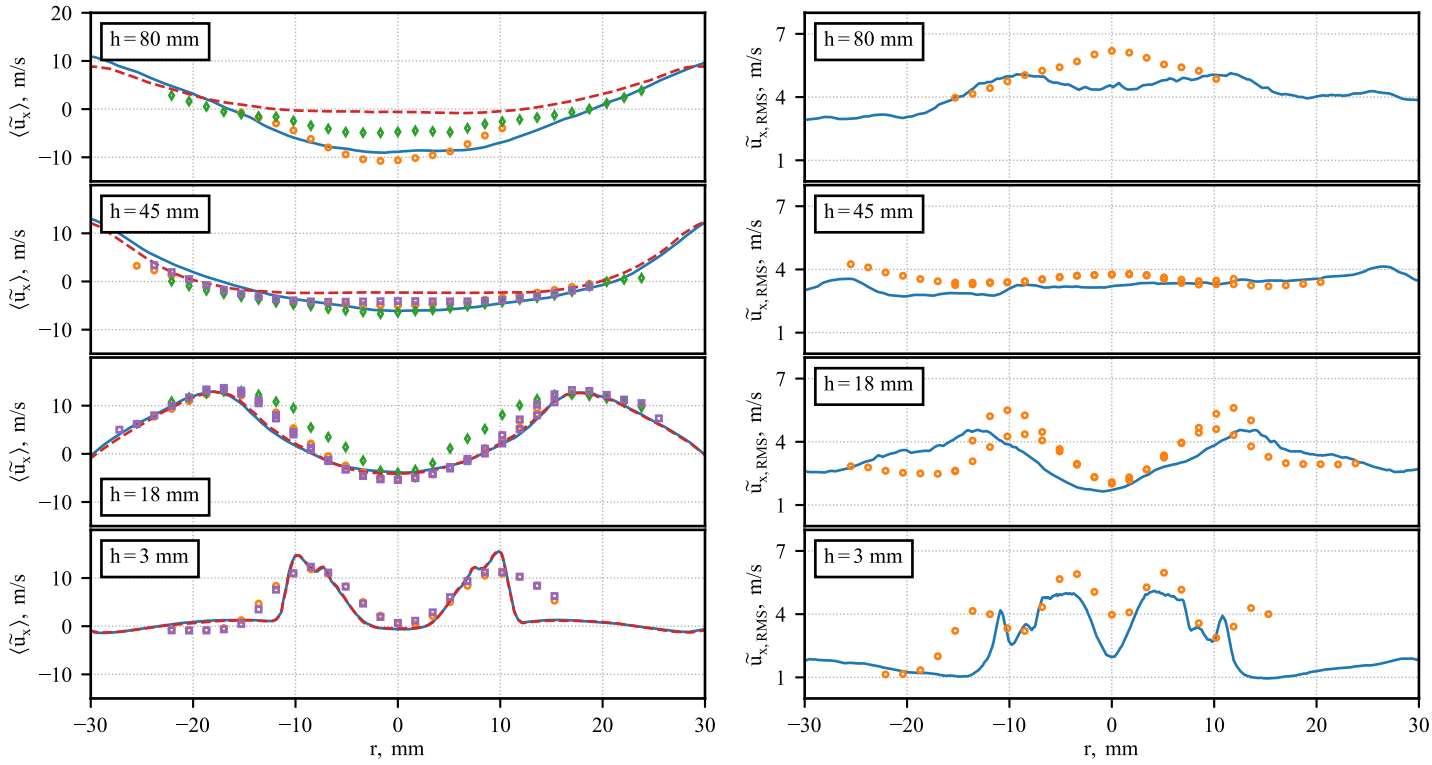

Figure 3: Radial profiles of the experimental [12] (PIV) and the simulated (LES) axial velocity component for OP-1 and OP-3. Left: Mean, right: RMS. — LES OP-1, ○ PIV-FoV OP-1, ◇ PIV-SoC OP-1, - - - LES OP-3, □ PIV-SoC OP-3.

applies to the radial and tangential velocity components, which are shown in the supplementary material. Despite some smaller deviations, the overall agreement of these velocity components with the experiment is excellent.

In other numerical studies where the velocity profiles close to the injector are given [10, 26], similar deviations at $-10 > r > 10$ mm are observed. A grid studies did not affect these differences [10]. Accordingly, the overestimated opening angle at $h = 18$ mm is observed in many other numerical publications [10, 24, 26, 72], too. In conclusion, simulated and measured velocity profiles agree well within measurement uncertainties.

PVC-frequencies of 440-442 Hz in the experiment [5, 14] and 430 Hz in the LES [7] agree well, too. Recent measurements in an acetone diluted variation of OP-1 revealed the presence of a double helical vortex [14] in the fuel dynamics near the primary injector, which is also found in the LES. The measured low frequency dynamics of soot evolution [5] at OP-1 is observed in the LES [7], too. Hence, all modes which are important for the soot evolution at OP-1 [7] are predicted correctly by the LES. Since OP-2 and OP-3 do not differ fundamentally from OP-1, it is assumed that the simulation approach achieves good results there as well. However, implications from soot evolution

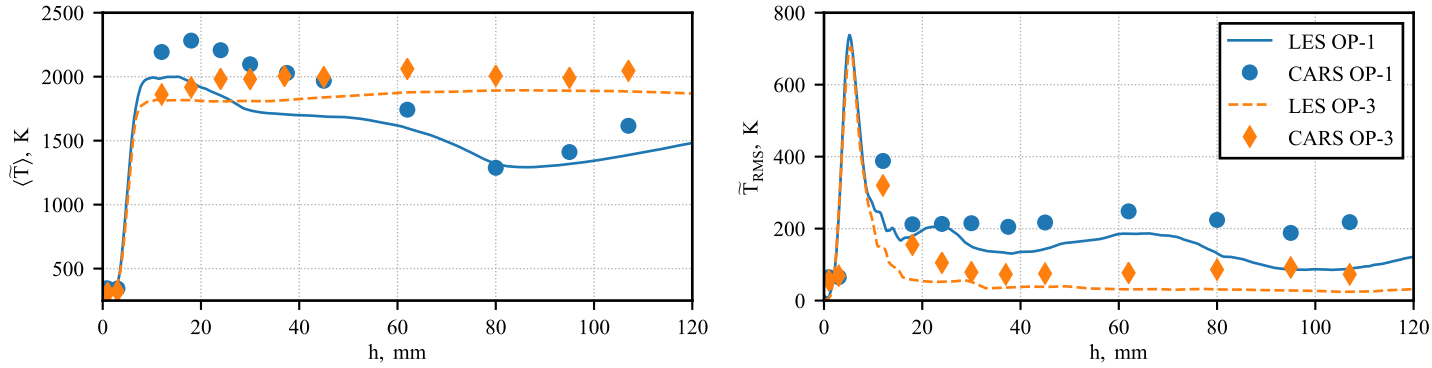

Figure 4: Experimental [9] (CARS) and simulated (LES) temperature on the axis for OP-1 and OP-3. Left: Mean, right: RMS.

mode analysis are limited by the capabilities of the soot model.

5.2. Flame shape

Figure 4 compares axial profiles of mean and RMS temperatures obtained by the LES and "coherent anti-Stokes Raman scattering" (CARS) measurements [9]. Close to the injector, the mean temperature strongly increases up to a height of $h \approx 10$ mm and the LES profiles are nearly identical. Further downstream differences appear between the OPs. At OP-1, mean temperature decreases towards the secondary air injection and slightly increases further downstream. In contrast, the temperature level for OP-3 remains nearly constant. The CARS measurements are in a good qualitative agreement with the simulation for both OPs. However, the LES underestimates the temperature level significantly in case of OP-1 and slightly for OP-3. Therefore, RMS values are too small in the LES as well. Simulation and experiment show the same behavior that the RMS values are constant in the IRZ.

Figure 5 compares radial temperature profiles. A very good agreement between the mean values is observed close to the injector ($h = 3$ mm), whereas the simulated RMS values are higher in the center of the combustor. This deviation indicates a slightly different position of the stagnation point between injected air and the IRZ. Since the deviations in the mean values are small, it is assumed that the general flame prediction quality of the LES is good. In the zone of primary combustion ($h = 18$ mm) a good quantitative agreement between experiment and LES is achieved. Differences concern the underestimated temperature on the axis by the LES and the overestimated opening angle of the V-shaped flame zone. Further downstream ($h = 45$ mm), simulated temperatures in the center of the combustor are lower than the measured ones. This disagreement vanishes for both OPs

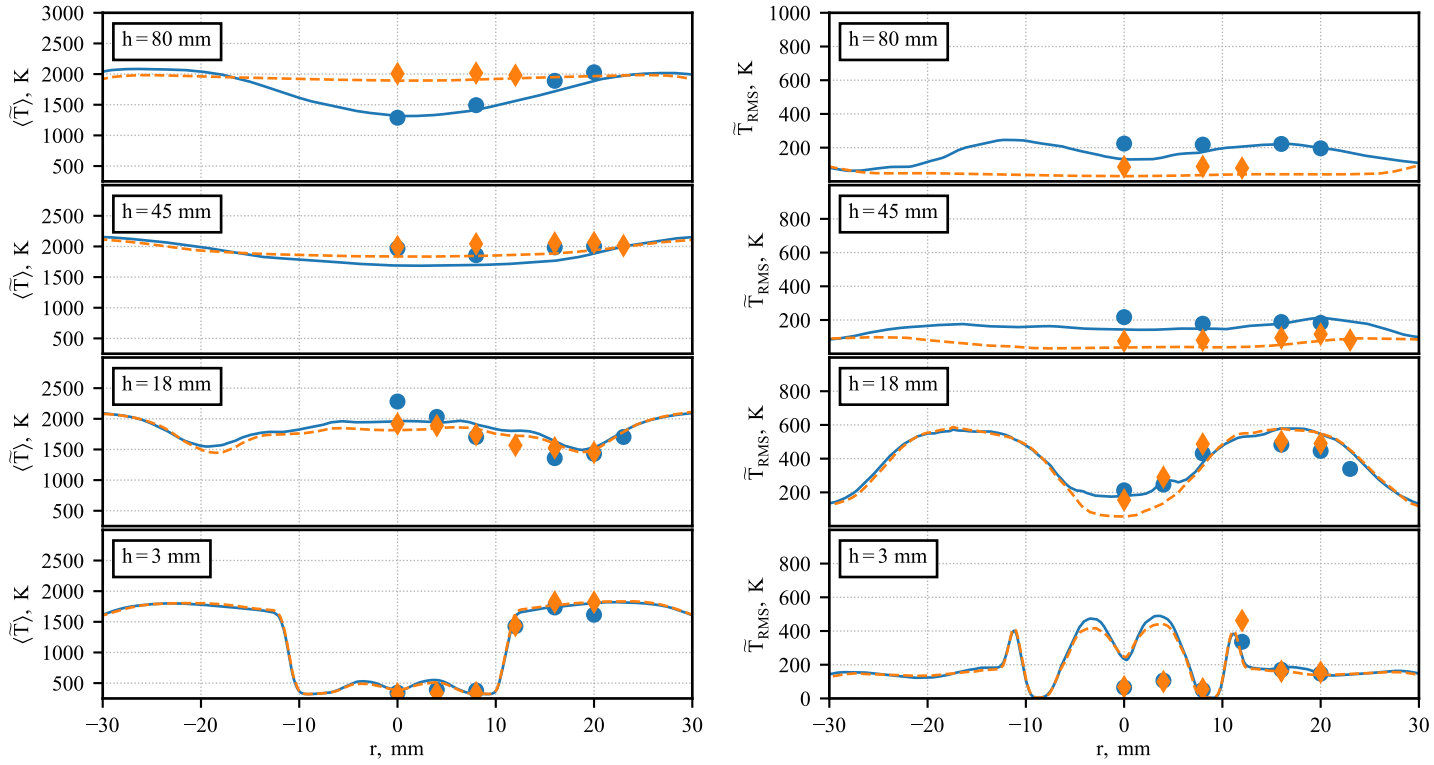

Figure 5: Radial profiles of the experimental [9] (CARS) and the simulated (LES) temperature. Left: Mean, right: RMS. — LES OP-1, - - - LES OP-3, ● CARS OP-1, ♦ CARS OP-3.

towards the periphery of the combustor. At the position of secondary air injection ($h = 80$ mm) the agreement of the mean profiles is good, while RMS is slightly underestimated by LES.

Figure 6 compares simulated and measured temperature histograms for OP-1 and OP-3. On the axis close to the injector ($h = 3$ mm, $r = 0$ mm) the histograms from LES show an almost entirely cold fluid, while about 10 % preheated fluid is found in the measurements. In the ORZ ($h = 3$ mm, $r = 20$ mm) the LES results of both OPs are almost identical and match the experimental data very well for OP-3. Even though the thermal power is higher for OP-1, experimental histograms are shifted towards lower temperatures. In the zone of primary combustion ($h = 18$ mm, $r = 0$ mm) the simulated statistics are shifted towards lower temperatures, while the shapes do not fundamentally differ from the measured histograms. In the outer part of the flame ($h = 18$ mm, $r = 20$ mm) temperature is almost uniformly distributed and the agreement between experiment and LES is excellent. Further downstream on the axis ($h = 45$ mm, $r = 0$ mm) the shapes of the histograms are predicted correctly by the LES, however shifted towards lower temperatures. The agreement improves towards the periphery of the combustor ($h = 45$ mm, $r = 20$ mm) while a small shift towards colder temperatures remains in the LES data. Close to the secondary air injection, at

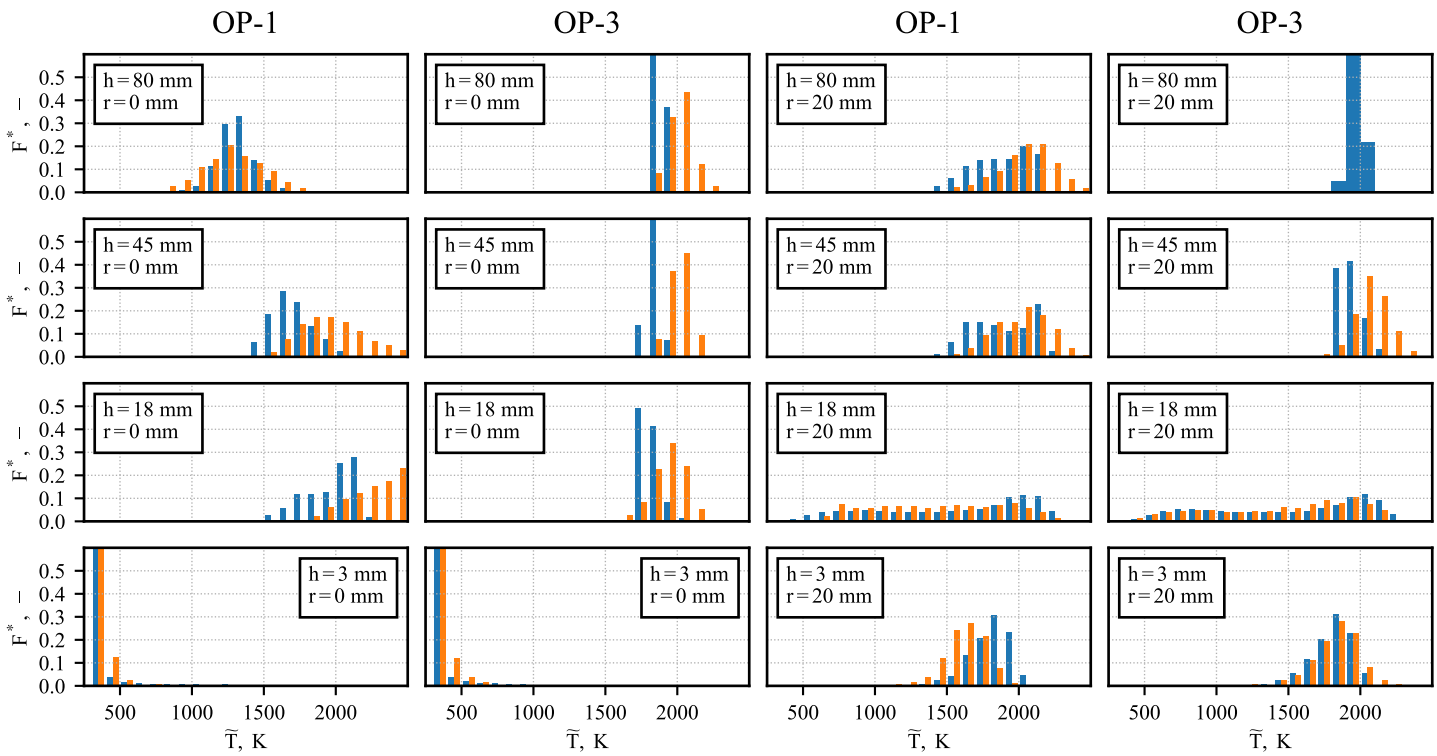

Figure 6: Histograms of the experimental [9] (CARS) and the simulated (LES) temperature for OP-1 and OP-3. — LES, — CARS.

$h = 80$ mm, the agreement is similar. While simulated temperatures are underestimated for OP-3 the agreement is good for OP-1.

The validation reveals, that the qualitative agreement between experiment and simulation is very good, while temperature is underestimated by the LES, especially in the IRZ. Overestimated heat losses due to a radiation model which neglects absorption might be the cause. However, the heat losses due to radiation are small compared to the heat losses due to wall heat transfer since soot concentrations are low in the AEMC [24, 72]. Even simulations which consider radiation absorption and detailed wall heat transfer models [24, 72] are not able to reproduce the measured temperatures accurately. Only in simulations where heat losses are completely neglected, the obtained temperatures agree with the experimental values in the region close to the injector [72]. Moreover, the CARS histogram on the axis ($h = 18$ mm, $r = 0$ mm) shows that 20 % of the measured temperatures for OP-1 are above the adiabatic flame temperature of 2424 K. Since radiative absorption is low in this part of the flame [72], further measurements would be helpful. Nevertheless, the simulated temperatures in this work are expected to be slightly too low, since 78 % of the emitted radiation should be absorbed within the combustor [72]. Hence, the overestimated radiative power can explain the

underestimated recirculation velocity in the IRZ. Lower temperatures cause higher densities, which, together with the underestimated velocity, have the effect, that the predicted recirculated mass flow should be similar as in the experiment. In conclusion, the flame shape is predicted sufficiently well by the LES, especially because the shapes of the histograms agree well for both OPs.

5.3. Soot prediction

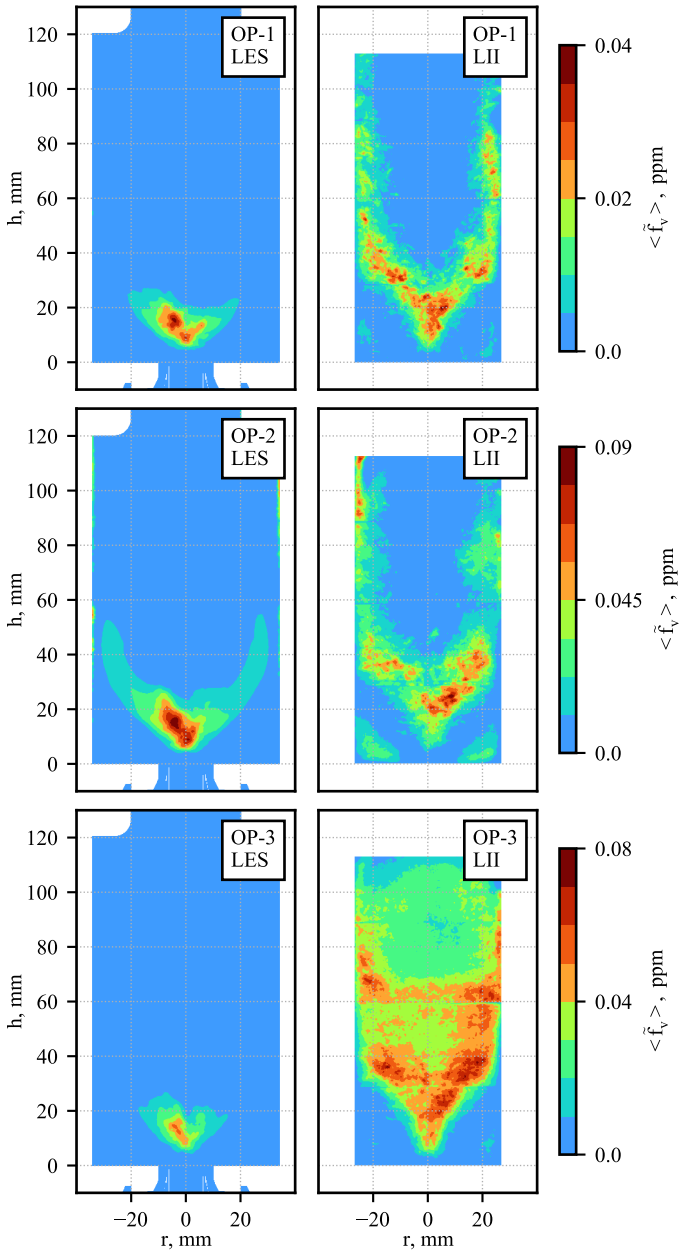

Figure 7: Calculated (LES, left) and measured (LII, right) [4] mean soot volume fraction at the investigated operating points.

Figure 7 shows the soot model performance by comparing measured (LII) and simulated (LES)

mean filtered soot volume fraction fields $\langle \widetilde{f}_v \rangle$ at the three operating points. Despite the comparatively long sampling time of 300 ms, asymmetries in the simulated soot fields persist, which can be attributed to strong soot intermittence. Temporal fluctuations of $\langle \widetilde{f}_v \rangle$ converged below typical soot modelling uncertainties, which allows a discussion on the magnitude of soot volume fraction. An additional comparison of PDFs [73] could confirm this, however, experimental PDFs of $\widetilde{f}_v$ are not available. This is why only $\langle \widetilde{f}_v \rangle$ is validated subsequently.

Most important, the influence of operating conditions on the $\langle \widetilde{f}_v \rangle$ magnitude near the injector is predicted well by the LES: Least soot is found at OP-1, while increasing the local or the global equivalence ratio raises the soot level by a factor of more than two, respectively. The difference in maximum soot volume fraction between LES and experiment is less than a factor of 1.5. For all OPs investigated, the soot level predicted in the injector region by the current LES very good compared to other state of the art LES of this flame from literature (e.g., [10, 21, 23, 27]). In the downstream part of the combustor, the differences between simulation and experiment are striking. While LII shows soot presence at the periphery of the combustion chamber at all OPs and in the IRZ at OP-3, the soot level in the LES is orders of magnitudes lower there. The LES performs best for OP-2, where soot presence at the periphery of the combustion chamber is clearly visible and in the same order of magnitude as in the experiment. In contrast to OP-2, operating conditions of OP-1 and OP-3 are close to the sooting limit ($ER_\mathrm{p} = 1.2$). The clearly better soot prediction of OP-2 illustrates the great difficulties that such conditions provide for soot modeling. To the authors knowledge, no LES except one with a simple, C_2H_2-inception based soot model [17], predicts a significant amount of soot in the IRZ for OP-3. This emphasizes, that state of the art soot models still involve large uncertainties, especially when applied on difficult conditions close to the sooting limit. Due to these uncertainties and the subsequent deviations between simulation and experiment, a further discussion on soot prediction is necessary before a meaningful soot formation analysis can be performed.

5.4. Soot evolution in the AEMC

Instead of being formed permanently, soot inception and growth i.e. soot formation in the AEMC is restricted to fuel-rich pockets which sporadically appear close to the inner shear layer [5, 25], where not only turbulence but also the PVC alternate the flow field [8, 9]. OH, PAH and soot measurements of Geigle et al. [11] indicate that soot forms near the primary injector, while soot presence at the periphery and the IRZ is due to transport. This suggests that soot formation is

predicted acceptably well by the LES while soot vanishes too fast in zones where soot transport should be dominant. The following statistical analysis of the mixing process in the AEMC further investigates this assumption since mean values are not sufficient to draw this conclusion in such a complex configuration.

Figure 8a-c present joint histograms of filtered temperature-equivalence ratio ($\widetilde{T}$, $\widetilde{ER}$) statistics which are insensitive to soot modeling errors and spatial coexistence of soot growth and oxidation. In turn, soot evolution strongly depends on local temperature and mixture (e.g. [32, 45]). Note that subgrid scale fluctuations can't be considered in the following analysis. This is not expected to affect the conclusions, since the level of turbulence is only moderate in the AEMC. The $\widetilde{ER}$ is calculated via the local filtered mixture fraction $\widetilde{Z}$ and the stoichiometric mixture fraction Z_{st} as $\widetilde{ER} = \widetilde{Z}/(1-\widetilde{Z}) \cdot (1-Z_{st})/(Z_{st})$. Soot formation in laminar premixed flames starts at about $ER > 1.7$ (e.g., [74]) which serves as a reference for the sooting tendency in the following discussion. Brown dashed lines for $\widetilde{ER} = 1.7$ indicates which part of the joint histogram covers soot formation promoting conditions. Contour plots colors indicate the probability of an event within a $\Delta\widetilde{ER} = 0.08$, $\Delta\widetilde{T} = 44$ K area of the $\widetilde{T}$-$\widetilde{ER}$ space. The statistical data are sampled between $1 < h < 110$ mm and $r < 30$ mm over the entire LES runs. Thereby, most of the combustor is covered and wall effects on the statistics are reduced.

Figure 8 shows that most frequent events are observed close to the primary and the global equivalence ratio. The probability of events with a high sooting propensity ($\widetilde{ER} > 1.7$) is low at all OPs. Without secondary air injection (OP-3), more fuel rich events at lower temperatures are observed compared to OPs with secondary air injection. In order to identify those regions in the combustor where the conditions favor soot formation, statistics are re-computed in segments of the AEMC which are shown in Fig. 8d). Hot, fuel-rich events, which promote soot formation, are found for all OPs only close to the injector and in the lower part of the periphery of the combustion chamber. In case of OP-2 the number of fuel rich events increases due to the increased fuel mass flow. Deactivating the secondary air injection increases the number of soot formation promoting events near the injector, only. In contrast to soot inception, soot growth can appear at fuel rich conditions with $\widetilde{ER} < 1.7$. Here, the effect of the operating conditions is the same as for $\widetilde{ER} > 1.7$. Therefore, soot inception and growth are similarly affected by the operating conditions which allows an analysis of soot formation as a whole.

In conclusion, the analysis of joint temperature-equivalence ratio statistics complements numerical [6] and experimental [11] studies of OP-1. Soot presence in the periphery of the combustor is

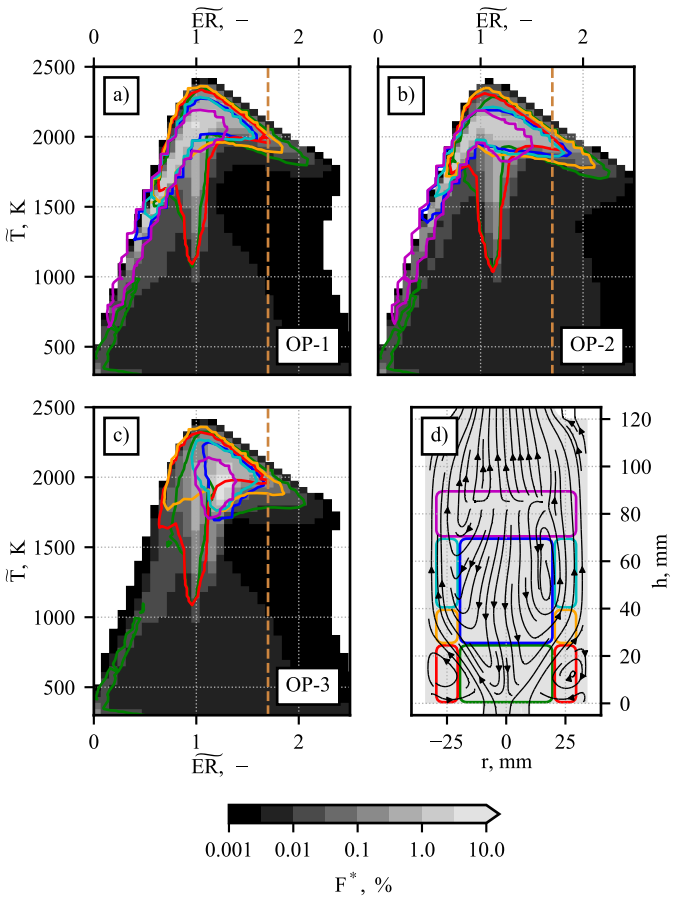

Figure 8: Joint histograms of normalized event probability F^* depending on temperature $\widetilde{T}$ and equivalence ratio $\widetilde{ER}$, for the investigated operating points a)-c). Smoothed iso-contours drawn at $F^* = 0.1\%$, spatially conditioned on the sampling positions shown in plot d): — injector, — IRZ, — ORZ, — peripheryDown, — peripheryUp, and — 2nd air. — streamlines, - - - $ER = 1.7$.

only possible due to soot transport, what also applies to OP-2 and OP-3. Events that promote soot formation are unlikely to happen there. Consequently, the predicted rapid soot decrease in the periphery is not linked to soot formation. Moreover, a much better soot prediction for the fuel rich OP-2 indicates a high sensitivity of the soot model to conditions close to the sooting limit, where OP-1 and OP-3 are operated. In summary, all relevant soot formation characteristics of the AEMC are covered by the current approach. Hence, even though soot evolution is not entirely predicted correctly, an analysis that is restricted to soot formation is possible.

6. Mode analysis

Figure 9a shows the temporal evolution of the total soot volume $\iiint \widetilde{f}_v dV$ in the AEMC. All OPs exhibit a very intermittent sooting behavior which has been observed in experimental investigations of OP-1, too [5]. The under-prediction of transported soot by the LES at all OPs may affect the relative differences in magnitude. However, absolute differences and the trend between the OPs are expected to be less affected. While soot volume magnitude approximately varies by a factor of five at OP-1, the variation is decreased at OP-2 to a factor lower than three. Both cases share secondary air injection which has been identified to affect the recirculated mass flow which causes such intermittence [7]. Unexpectedly, the soot volume intermittence magnitude does not decrease without secondary air injection. At OP-3 soot volume varies by a similar factor as at OP-1. While the amplitude constantly changes at OP-1 and OP-2, a more bimodal behavior is observed for OP-3. PDFs of the soot volume, calculated by kernel density estimation, are shown in Fig. 9b and quantify this difference. Despite different magnitudes, a bell-shaped PDF is observed for the cases with oxidation air (OP-1, OP-2) while the OP-3 PDF shows a bimodal like distribution with two local maxima. An explanation of the observed influences of the operating conditions on soot requires a thorough mode analysis.

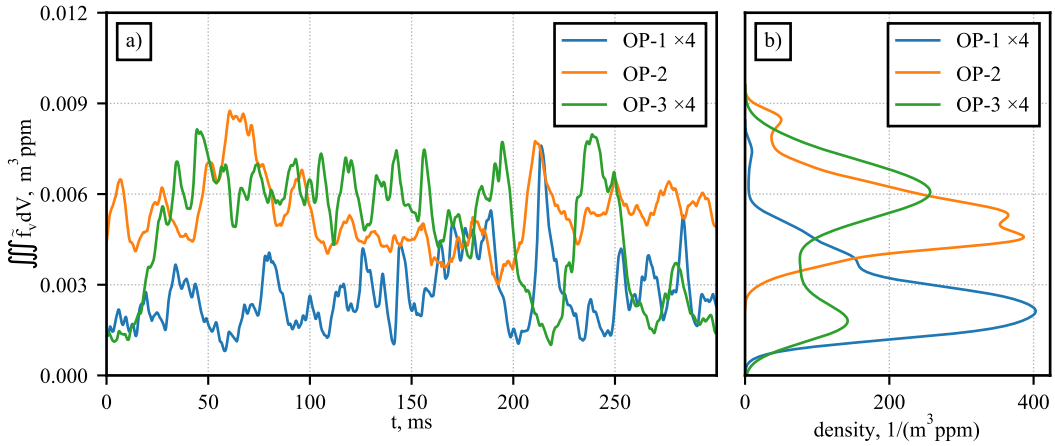

Figure 9: Temporal evolution (left) and PDF (right) of integrated soot volume fraction in the AEMC.

Figure 10 presents the band-pass filters which are used to separate different dynamics. They cover the LFD, the PVC, its first harmonic (2PVC) and higher harmonics (3PVC). Restrictions in filter design prevented a more appropriate filter that fully covers the second PVC harmonic. The remaining frequency band between LFD and PVC is called semi-LFD (SLFD). Hence, the complete frequency band is covered by the filters, which allows for a meaningful energy content comparison.

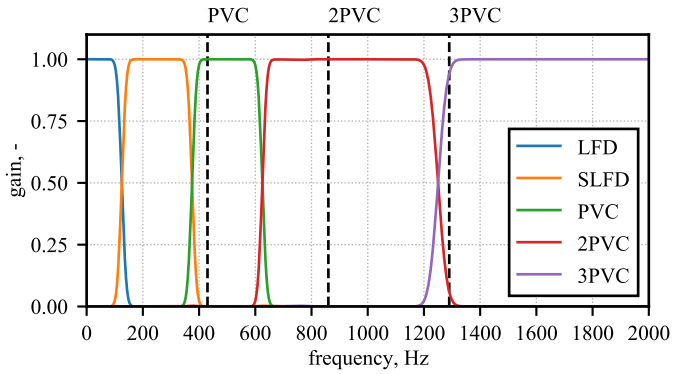

Figure 10: Filter gain of the band-pass filters used for MRPOD.

6.1. Energy content of modes

Figure 11 compares the normalized energy content E^* (Eq. 12) of velocity (u'), mixture fraction (Z'), PAH (Y'_{PAH_1}) and soot (f'_v) modes with the highest energy contents at all OPs. The total energy content $E_{tot} = \text{trace}(\mathbf{K})/N$ is given for each variable to compare absolute values, too. Since the entire computational domain is used for mode analysis, the energy content of the modes is lower as in comparable measurements in a spatially more restricted cut-plane [14]. In accordance with experimental observations at OP-1 [14], LES results of all OPs show that the PVC is the flow field dynamic which contains the most energy. The coherent mode pair is identified by their similar energies. Compared to non-reacting simulations, combustion slightly rises the normalized PVC energy, which is highest at OP-3. However, the PVC energy magnitude is almost identical at all OPs since secondary air injection nearly doubles the total kinetic energy in the combustor. Second most energy is contained in the first LFD modes, which appear incoherent except for the non-reacting case at OP-1, where the first two modes show nearly identical energies. Combustion at OP-1 causes a destruction of the coherent LFD dynamics and their energy gets unevenly distributed over the first LFD modes. No coherent LFD dynamics are present at the OP-3/NR. $E^*(u')$ of the first LFD modes is much higher for cases with oxidation air than without. Modes in other frequency bands have a low contribution to the total flow field energy.

$E^*(Z')$ is distributed differently. As for the flow field, the most energetic mixture fraction dynamic at all OPs is the PVC. However, the energy content of the 2PVC mode pair of the mixture fraction field is considerably higher than in the other fields. The coherent structure in this frequency range is a double helical vortex (DHV), which is also observed in the experiment [14]. It appears particularly strong in the mixture fraction field since the highest changes are located in the region close to the injector, where the DHV is strongest. This also explains the high normalized energy

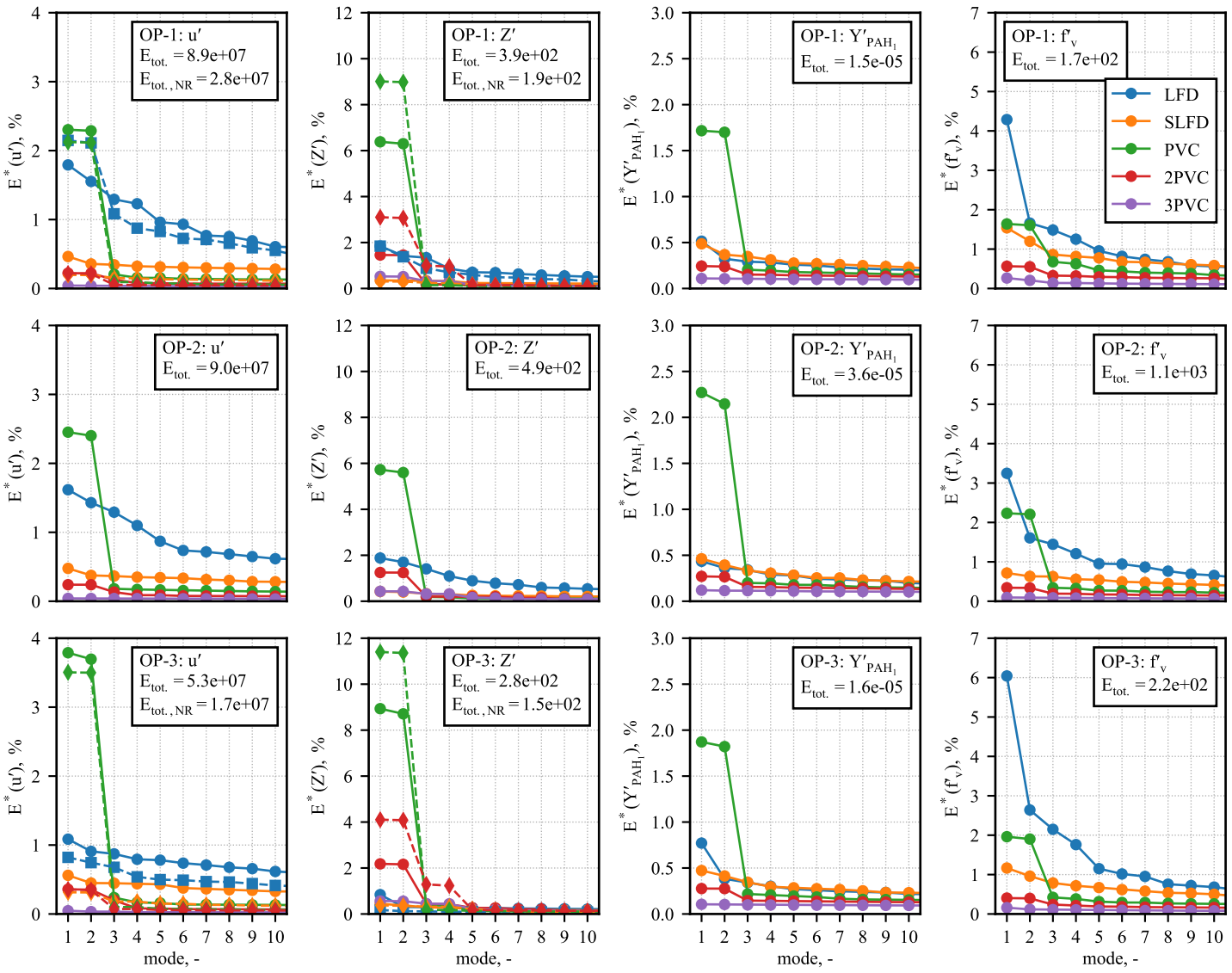

Figure 11: Normalized energy content E^* of velocity (u'), mixture fraction (Z'), mass fraction of the first PAH section Y'_{PAH_1} and soot volume fraction (f'_v) MRPOD modes. Circles belong to reacting, diamonds and squares to non-reacting simulations. Colors indicate MRPOD filters. Lines serve as a guidance for the eye.

content of the PVC mode without secondary air injection. The total energy content of the PVC mixture fraction modes at OP-1 and OP-3 is identical while these modes contain slightly more energy at OP-2 as more fuel is injected.

Modes of the first PAH section show a similar behavior, while the energy difference is increased. The energy distribution reveals, that findings concerning OP-1 [7] hold for OP-2 and OP-3 as well: All dynamics other than the PVC have a small influence on the PAH dynamics. Acetylene, the other major soot precursor, is affected in the same way (not shown).

The impact of the PVC on soot volume fraction is reduced compared to its influence on the

soot precursors. Due to the intermittent soot volume content in the combustor, the first soot LFD mode contains substantially more energy than the other modes. The correlation between $\iiint \widetilde{f}_v dV$ and $a_{1,LFD}(f'_v)$ already has been shown for OP-1 [7]. Total soot energy content reflects the previously described differences in soot volume: The primary equivalence ratio has a huge impact on soot formation, while the influence of secondary air injection is lower. However, the absence of secondary air injection increases the normalized energy content of $a_{1,LFD}(f'_v$. Despite the dominant soot intermittence, the PVC also contains a considerable amount of energy at all OPs, showing its relevance for soot evolution. In conclusion, the most important dynamics at all OPs are the PVC and LFD. They are subsequently analyzed further, in order to clarify the influence of the chosen operating conditions.

6.2. PVC influence on soot formation

The PVC is a helical vortex emerging from the inner air nozzle of the primary injector. It is commonly observed in combustors with swirled primary injection (e.g., [75]). In flames similar to the investigated ones, PVC intensifies fuel-air mixing at the ISL [14, 76]. Soot formation at OP-1 is affected by the PVC [8, 12] such that soot filaments are transported and that the enhanced mixing promotes soot formation [7, 25]. Mode energies revealed a very similar PVC presence in the flow field of all OPs, whereas its impact on soot precursors and soot formation is very different in absolute numbers.

Figure 12 analyzes the influence of the OPs on the equivalence ratio near the primary injector. The mean $\widetilde{ER}$ classifies the sooting propensity. In case of OP-1 soot promoting conditions ($\langle\widetilde{ER}\rangle > 1.7$) are found in the vicinity of the injector only, while the conditions at the ISL are not rich enough to promote soot formation continuously. The same holds for OP-3, at which the $\langle\widetilde{ER}\rangle$ in the IRZ is slightly increased but not beyond $\langle\widetilde{ER}\rangle = 1.7$. Only OP-2 provides conditions that clearly promote soot formation at the ISL. The absence of such conditions at OP-1 and OP-3 illustrates that these operating conditions are close to the sooting limit. PVC influence on the $\langle\widetilde{ER}\rangle$ field is shown in Fig. 12 by reconstructing the equivalence ratio for an exemplary timestep (Eq. 10) in a horizontal cut plane at $h = 10$ mm. As already observed in the results for $E^*_{PVC}(Z')$, the PVC influence on the $\langle\widetilde{ER}\rangle$ is similar for all OPs. The PVC promotes mixing and subsequently soot formation conditions at the ISL for all OPs. At OP-2 they cover almost the entire circumference, while less fuel-rich conditions prevail at OP-1 and OP-3. Due to secondary air injection, the soot formation promoting areas at OP-1 are slightly smaller than at OP-3. In conclusion, PVC influence on fuel-air mixing is

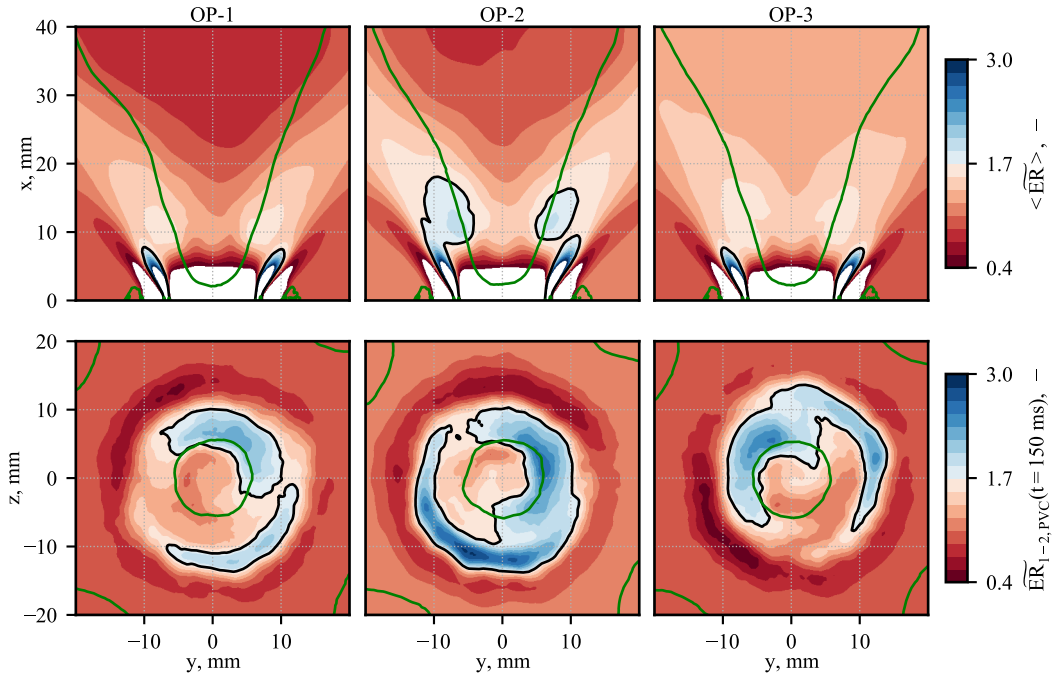

Figure 12: Top: mean equivalence ratio field in a vertical cut plane at z=0 mm. Bottom: mean equivalence ratio field superimposed by reconstructed equivalence ratio PVC at an exemplary time step of $t = 150$ ms (Eq. 11) in a horizontal cut plane at x=10 mm. — $\langle \widetilde{u}_x \rangle = 0$ m/s, — $\widetilde{ER} = 1.7$.

found to be crucial for soot formation.

In contrast to the conservative variable $\widetilde{Z}$, species mass fractions are changed by chemical reactions in addition to transport and diffusion. These processes can't automatically be distinguished by POD. In order to separate PVC influence nevertheless, Grader et al. [7] analyzed phase shifts between temporal coefficients of two variables. However, these phase shifts are not well defined. Thus, a global analysis of the temporal coefficients phase shift is invalid. For these reasons an analysis of the local phase shift $\Delta\tau(x, \alpha', \gamma')$ (Eq. 13) of reconstructed PVC modes is proposed in this paper. By using reconstructed modes instead of temporal coefficients, phase shifts remain well defined. In addition, the local analysis provides a more detailed insight into the PVC effects on chemistry. Given that one variable (α') is representative for the PVC, $\Delta\tau$ reveals the local PVC influence on the other variable (γ'). Since Z' reflects the mixing influence of the PVC, it is chosen as the representative variable ($\alpha' = Z'$). The mean phase shift is interpreted such that values of $\Delta\tau \approx 0°$ and $\Delta\tau \approx 180°$ indicate that the PVC instantly increases or decreases γ', respectively. This can be due to transport e.g. when the flame front is moved by the PVC, or could be a consequence of very fast chemistry. Values in between indicate a temporal shift between the PVC mixing and a change in γ'. This delay is interpreted as a consequence of slow chemical reactions. Such

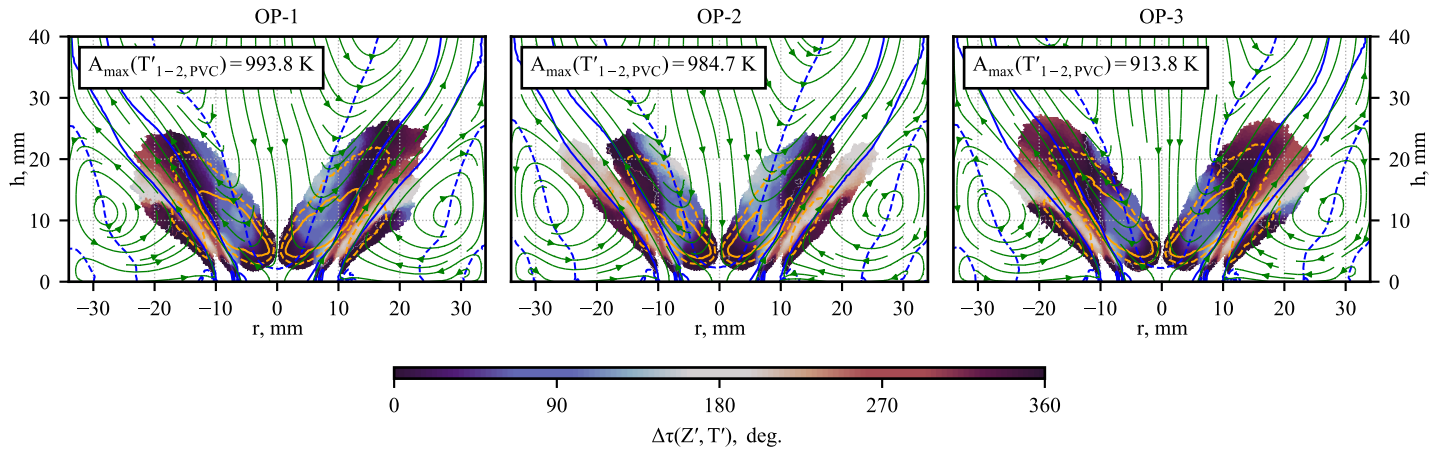

Figure 13: Phase shift $\Delta\tau$ of reconstructed PVC-filtered modes of Z' and T'. $\langle\widetilde{u}_x\rangle = 10\ m/s$, $\langle\widetilde{u}_x\rangle = 0\ m/s$, $2/3 \cdot A_{max}(T'_{1-2,PVC})$, $1/3 \cdot A_{max}(T'_{1-2,PVC})$, streamlines. Contour is drawn for $A > 0.1 \cdot A_{max}$.

comparatively slow reactions are typical for soot chemistry.

Figure 13 shows $\Delta\tau(Z', T')$ distributions close to the injector for all OPs. Streamlines reveal, that in all cases the major PVC impact on temperature is located in the region between the IRZ and the ORZ. The magnitude of the PVC influence is indicated by its transient amplitude $A(\alpha'_{1-2,PVC}(x,t)$. The maximum amplitude of PVC-related temperature fluctuations in the combustor $A_{max}(T')$ is highest for OP-1 and decreases as ER_g rises. Iso-contours show, that the highest temperature amplitudes are found near the ISL close to the injector for all OPs. Both major flame fronts are located close to the core of the main flow (solid blue lines) in the ISL and the OSL. A mean phase shift of $\Delta\tau(Z', T') \approx 0°$ and $\Delta\tau(Z', T') \approx 180°$ indicates that the PVC just moves the flame fronts at these locations. As already discussed, cold fuel-rich pockets are formed by the PVC which mix with the recirculated hot gas near the IRZ. Here, the phase shift between PVC mixing and temperature is about 90 degree and temperature amplitudes are highest. Hence these temperature fluctuations are not due to instant transport or mixing but due to slow chemical reactions. The high magnitude of temperature amplitude is an effect of the combustion of the cold gas. All OPs show this behavior similarly. This demonstrates, that the different operating conditions can change the strength of the PVC influence while they do not affect the general mechanism how PVC influences combustion. Thus, the PVC mixing impact on soot formation is subsequently analyzed for OP-1 only.

Figure 14 shows distributions of the phase shift $\Delta\tau$ between the PVC and $Y'_{C_2H_2}$ (left), Y'_{PAH_1} (middle) and f'_v (right), respectively. Acetylene is the most important soot growth species in this flame [10]. Its phase shift to the PVC is almost zero between the inner and outer shear layer,

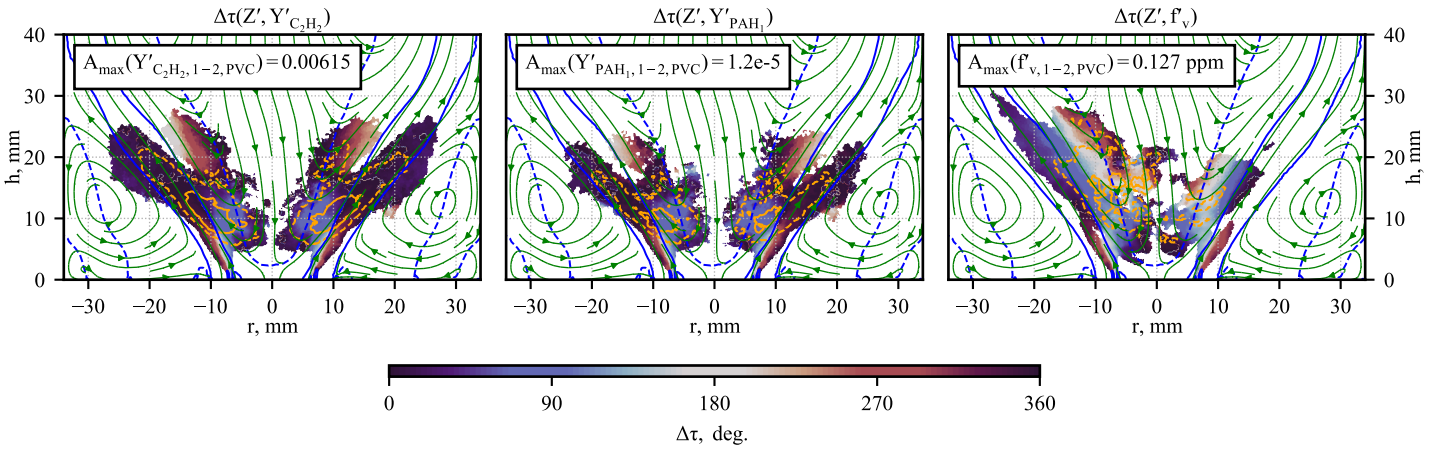

Figure 14: Phase shift $\Delta\tau$ of reconstructed PVC-filtered modes of Z' and $Y'_{C_2H_2}$ (left), Y'_{PAH_1} (middle) and f'_v (right) at OP-1. — $\langle\widetilde{u}_x\rangle = 10\ m/s$, - - - $\langle\widetilde{u}_x\rangle = 0\ m/s$, — $2/3 \cdot A_{max}$, - - - $1/3 \cdot A_{max}$, — streamlines. Contour is drawn for $A > 0.1 \cdot A_{max}$.

which means that the PVC does not affect acetylene chemistry here. Near the IRZ, close to the injector, the phase shift increases and high amplitudes of acetylene are found. Hence, PVC induced chemical reactions have a significant impact on acetylene concentration in the IRZ. PVC mixing impact on PAH is very similar to its impact on acetylene, even though PAH dynamics are slightly shifted away from the main flow towards the IRZ close to the injector. In this region, $\Delta\tau(Z', f'_v)$ is larger than the phase shift between PVC and soot precursors. This indicates slow soot chemistry. Further downstream, the phase shift decreases but does not disappear. Since soot precursors are in phase with the PVC there, the small phase shift in soot shows that it is mainly transported by the PVC but grows weakly at the same time, too. In conclusion, the PVC induced mixing results in slow chemical reactions in a small zone near the ISL close to the injector, leading to growth of soot precursors and soot. Close to the main flow and the flame fronts, soot and soot precursors are mainly transported by the PVC. Previous findings [7] are confirmed by this study and now extended to all OPs.

Table 2 compares the standard deviations of the normalized PVC amplitudes of relevant variables. Previous studies of OP-1 [7], which found an almost constant amplitude for mixture fraction and a highly fluctuating one for soot volume fraction, are confirmed. OP-2 and OP-3 show the same behavior. In all cases, the PVC amplitudes of velocity, temperature and mixture fraction are almost constant. The largest PVC amplitude fluctuations are found for the soot volume fraction. Cross-correlation (not shown) reveal a clear connection between the PVC amplitudes of soot and

$\sigma(A) \cdot 10^3$	u'	T'	Z'	$Y'_{C_2H_2}$	Y'_{PAH_1}	f'_v
OP-1	3.5	3.5	2.5	4.6	6.2	21.4
OP-2	3.0	3.2	2.6	3.6	4.3	13.1
OP-3	3.1	3.6	2.9	4.0	5.1	18.1

Table 2: Standard deviations of the amplitudes ($\sigma(A)$) of the eigenvectors $\Psi_{1,PVC}$.

the first LFD mode of soot for all OPs. Soot precursor amplitudes are much less fluctuating than $A(\Psi_{1,PVC}(f'_v))$ what confirms their insensitivity with respect to the LFD. OP-2 shows significant smaller amplitude fluctuations, especially for the soot volume fraction. Hence, the higher equivalence ratio at the primary injector decreases the sensitivity of the soot formation mechanisms in the AEMC on LFD.

6.3. LFD analysis - mixture fraction field

Even though the PVC enables soot formation in the combustor, its steady motion can't explain the intermittent soot dynamics. Low frequency dynamics in the velocity and mixture fraction field have been identified to cause the soot intermittence at OP-1 [7]. Strictly speaking, a coupling between the recirculated mass flow and secondary air jet flapping with the mixture fraction was found as well as a coupling between mixture fraction and soot. Such an LFD mode with significant impact on the flame has been reported in other swirl combustors as well [77] and is called "shift mode". The LFD analysis is extended subsequently to all operating points including non-reacting simulations. Thereby a more comprehensive understanding of the shift mode and the influence of the operating conditions will be achieved.

Figure 15 compares all investigated operating points by means of the most energetic axial velocity LFD mode $\Phi_{1,LFD}(u'_x)$. Particularly interesting is the mode at OP-1/NR since the analysis of kinetic energies (see Fig. 11) revealed that $\Phi_{1,LFD}(u'_x)$ and $\Phi_{2,LFD}(u'_x)$ form the only pair of coherent LFD modes at all investigated cases. It acts on the secondary air injection, the recirculation zone and the primary injector in such a way that the motion is opposed in the left and right half of the combustor. No comparable mode is observed without secondary air injection (OP-3/NR), indicating that this coherent motion is caused by the flapping of the secondary air jets. Conversely, the most energetic mode of OP-3/NR affects the downstream parts of the combustor only weakly. Its shape is axially symmetric instead and the magnitude is strongest near the injector, alternating the axial position of the V-shaped injected gases. The influence of combustion on $\Phi_{1,LFD}(u'_x)$ is

significant. In OP-1, the influence of the secondary air jet becomes weaker and the mode hardly acts on the primary injector while it maintains its influence on the recirculation zone. This mode occurs similarly at OP-2. At both OPs, $\Phi_{2-4,LFD}(u'_x)$ also contain features of the coherent mode pair from OP-1/NR and a significant amount of energy (not shown). Hence, combustion disturbs the coherent jet flapping mode and redistributes this motion in at least four incoherent modes with similar energy. In a previous investigation [7] of OP-1, one of these modes was found to be axially symmetric. It corresponds to $\Phi_{4,LFD}(u'_x)$ in the present work. Without secondary air injection and with combustion, the axially symmetric $\Phi_{1,LFD}(u'_x$ mode at OP-3 is weaker, but still present.

Figure 16 compares $\Phi_{1,LFD}(Z'_{inj.})$ obtained by MRPOD in a volume close to the injector ($0 \leq h \leq 25$ mm and $r \leq 20$ mm). The spatial restriction is required to prevent disturbances by different dynamics of similar energy in other parts of the AEMC. Unlike the velocity LFD modes, the mixture fraction modes are very similar, even for the non-reacting cases. These modes act on the mixture fraction in most parts of the IRZ such that an increase of $a_{1,LFD}(Z'_{inj.})$ decreases the mixture fraction and vice versa. An area close to the shear layer below $h \approx 10$ mm is affected contrarily in a way that an increase in $a_{1,LFD}(Z'_{inj.})$ increases the mixture fraction. In OP-3, the upper part of the IRZ is less affected since no unburnt gas is recirculated. In the non-reacting cases, the contrary behavior is not as pronounced as in the reacting cases but still visible. Both reacting and non-reacting modes are virtually axially symmetric except those of reacting OP-1 where the mode, as the $\langle \widetilde{f}_v \rangle$ field (see Fig. 7), is less axially symmetric. Iso-contours of average soot source terms ($\langle \bar{\omega}_s \rangle$) illustrate, that soot formation occurs in spatial accordance with the negative part of the mode. The fact that the mode is present in all cases, underlines its importance even though its energy content is low ($E^*_{1,LFD}(Z'_{inj.}) < 1$ %).

Figure 17 presents the cross-correlation of the first four $a_{LFD}(Z'_{inj.})$ modes with soot volume $\iiint \widetilde{f}_v dV$ (top) and of $a_{1,LFD}(Z'_{inj.})$ with the first four $a_{LFD}(u'_x)$ modes under non-reacting (middle) and reacting (bottom) conditions. The correlation of the first mixture fraction mode with the soot volume in the combustor is significant for all OPs. Hence, $a_{1,LFD}(Z'_{inj.})$ is linked closely to the sooting behavior of the AEMC. This can be explained by the axially symmetric influence of $a_{1,LFD}(Z'_{inj.})$ in a region where soot formation is strongest. Only axially symmetric modes are expected to influence a global variable like the soot volume to such an extent. Asymmetric modes would mostly cancel out their effect on the global variable. The strong response of soot formation on small changes in mixture fraction exemplifies the highly nonlinear soot chemistry. Correlation of non-reacting OPs reveal the connection between the flow field LFD dynamics and $a_{1,LFD}(Z'_{inj.})$.

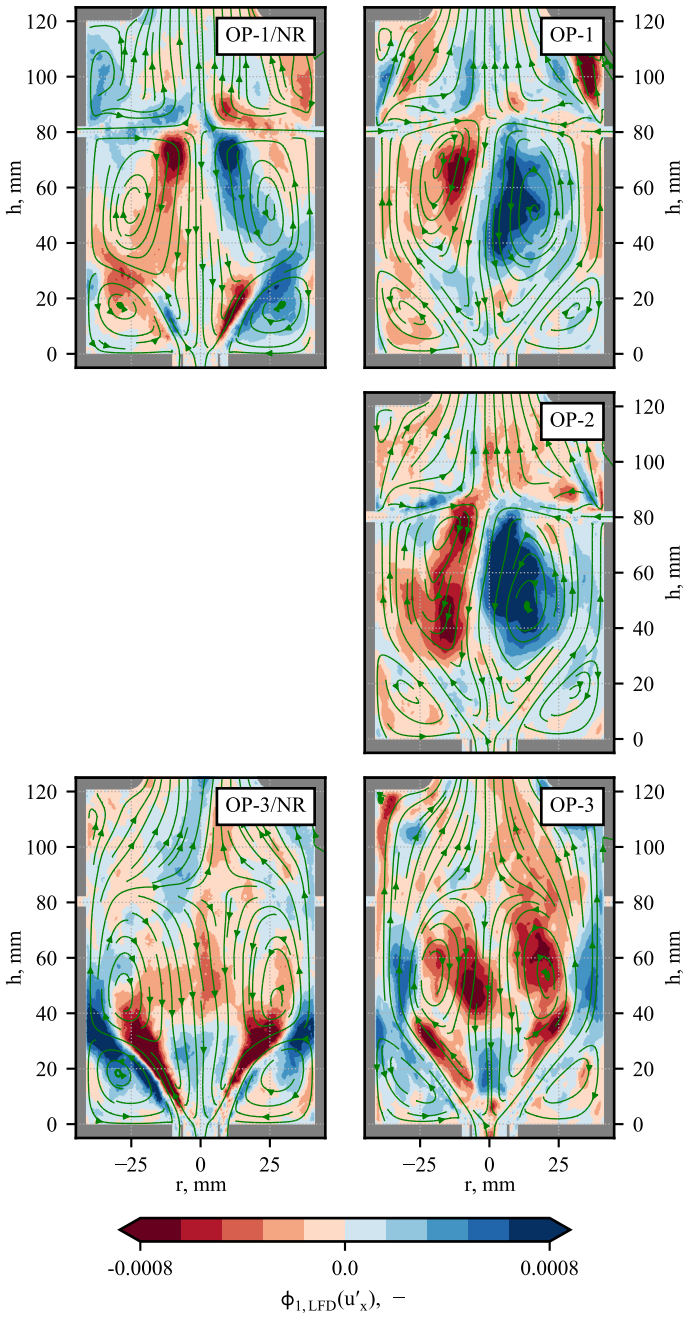

Figure 15: First LFD band-pass filtered spatial mode of axial velocity u'_x for all operating points, including non-reacting conditions. — streamlines.

In OP-3/NR a clear correlation between the axially symmetric $a_{1,LFD}(u'_x)$ and $a_{1,LFD}(Z'_{inj.})$ is found. Non-symmetric but coherent $a_{1-2,LFD}(u'_x$ of OP-1/NR show a weaker but still noticeable correlation with $a_{1,LFD}(Z'_{inj.})$. Yet, the highest correlation at OP-1/NR is between $a_{3,LFD}(u'_x)$ and $a_{1,LFD}(Z'_{inj.})$. This is the most energetic axially symmetric LFD mode in the flow field (not shown). The disturbing effect of combustion on the LFD is also visible in the cross-correlations

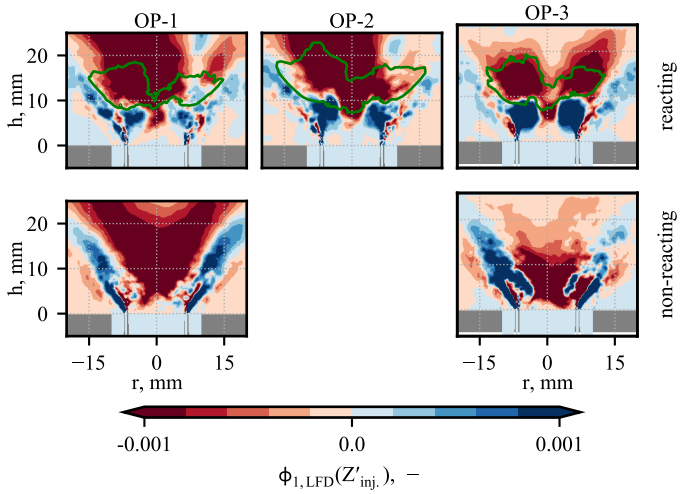

Figure 16: First LFD band-pass filtered spatial mode of the mixture fraction field close to the injector $Z'_{inj.}$ for all operating points, including non-reacting conditions. Iso-contour indicate the mean soot source term: — $1/3 \cdot \max(\langle\bar{\omega}_s\rangle)$.

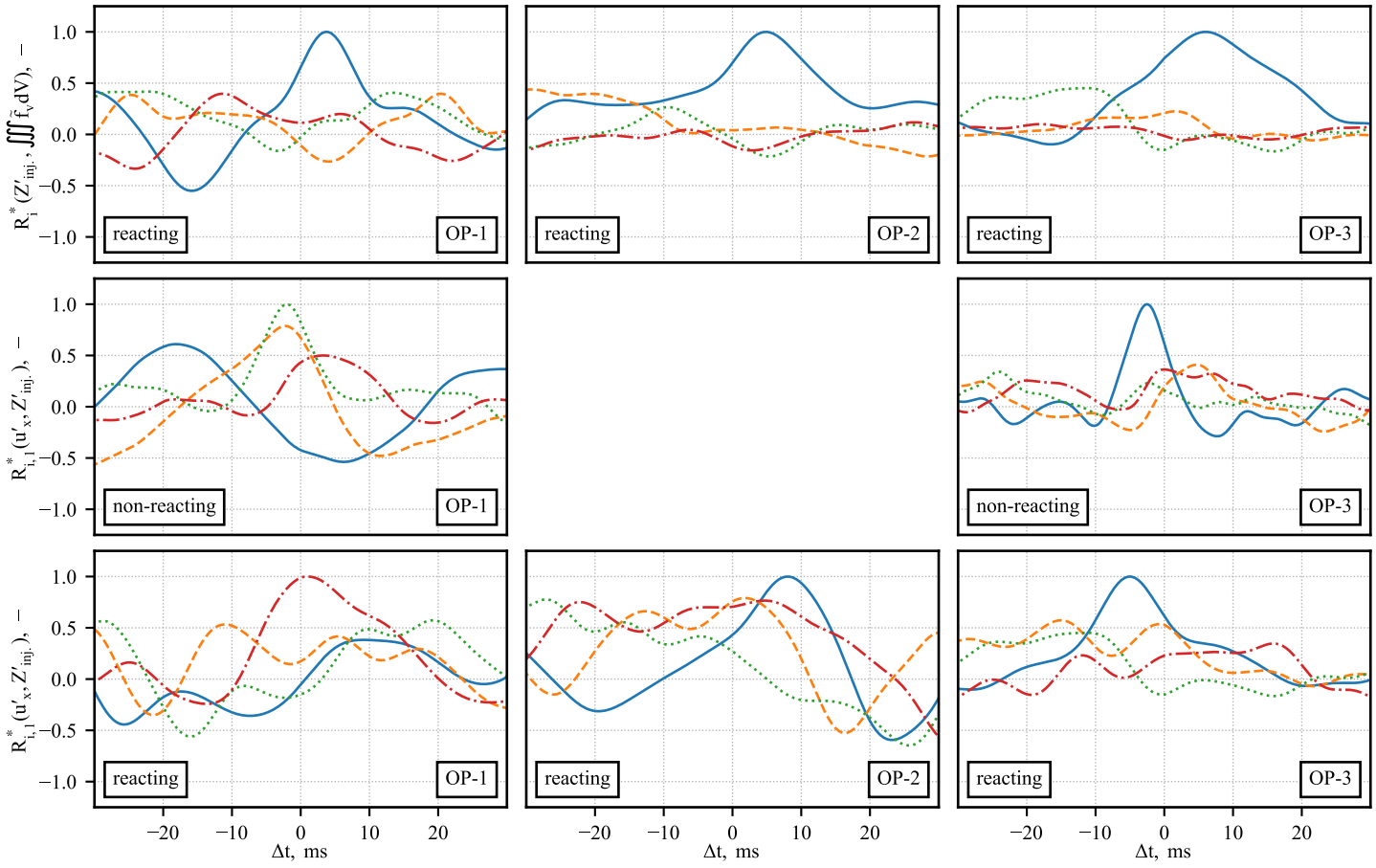

Figure 17: Normalized cross-correlation of LFD modes of mixture fraction with soot volume (top) and velocity for non-reacting (middle) and reacting conditions (bottom). — $i = 1$, - - $i = 2$, ····· $i = 3$, -·-· $i = 4$.

between $a_{1,LFD}(Z'_{inj.})$ and the first four $a_{LFD}(u_x)$ modes. Only the correlation of $a_{1,LFD}(u'_x)$ and $a_{1,LFD}(Z'_{inj.})$ at OP-3 is significantly higher than the other correlations. As shown in Fig. 15, this is the symmetric LFD mode. In OP-2 the first flow field modes weakly correlate with $a_{1,LFD}(Z'_{inj.})$. As previously reported [7] at OP-1, the axially symmetric mode correlates strongest. This is confirmed by the present study where $a_{4,LFD}(u'_x)$ is the most axially symmetric mode. Especially at OP-2 the combustion induced breakdown of the coherent jet flapping motion seems to prevent an axially symmetric LFD mode. Therefore, there is only a weak influence of all LFD modes on $a_{1,LFD}(Z'_{inj.})$. It can't be ruled out, that POD mode separation suffers from the similar energy content of the LFD modes at OP-1 and OP-2, which means that an axially symmetric mode could be present at OP-2 as well.

In conclusion, the intermittent sooting behavior is caused by an axially symmetric, incoherent LFD flow field mode which impacts the mixture fraction field close to the injector. The secondary air injection disturbs this axially symmetric mode and causes a more chaotic response of soot. This explains the different soot volume PDF shapes found in Fig. 9. As only one mode acts as a shift mode on soot at OP-3, a bimodal distribution like PDF is observed. The chaotic influence of the incoherent secondary air injection mode results in a Gaussian-like PDF at OP-1 and OP-2.

6.4. LFD Analysis - joint statistics

Mode analysis based on $a_{1,LFD}(Z'_{inj.})$ proofed to be successful and gave insight into the local soot formation dynamics. Even though a clear correlation between the first mixture fraction mode close to the injector and the sooting behavior was found at all OPs, the energy content of $a_{1,LFD}(Z'_{inj.})$ is very low and the analysis may unintentionally exclude further important modes. Therefore, previous conclusions are subsequently backed up by investigating a more general link between flow field dynamics and soot formation. The potential of joint statistics to provide a more global insights has already been demonstrated. As $\widetilde{ER}$-$\widetilde{T}$ statistics, sampled in the entire combustor, are not expected to change over time, a local analysis is conducted in the previously defined sampling locations (see Fig. 8d). At each location, MRPOD is applied to the temporal evolution of $F_t'^*(\widetilde{ER}$-$\widetilde{T})$ (Eq. 3). Statistically stationary phenomena, like turbulence or the PVC, are inherently excluded from the analysis so that the influence of LFD modes gets clearer.

Figure 18 presents the normalized Energy of $F_t'^*(\widetilde{ER}$-$\widetilde{T})$ modes sampled in the most relevant locations for soot evolution: near the injector, at the peripheryDown (pD) location and in the IRZ (see Fig. 8d). As expected, significantly more energy is contained in the first $F_t'^*(\widetilde{ER}$-$\widetilde{T})$ modes than

in the $Z'_{inj.}$ modes. Especially in the IRZ, the first mode contains more than 30 % of the energy. Near the injector and at the pD location, where soot formation can take place, the energy of the first mode is still above 15 % at all OPs. The influence of the first mode is further investigated since higher modes already contain significantly less energy.

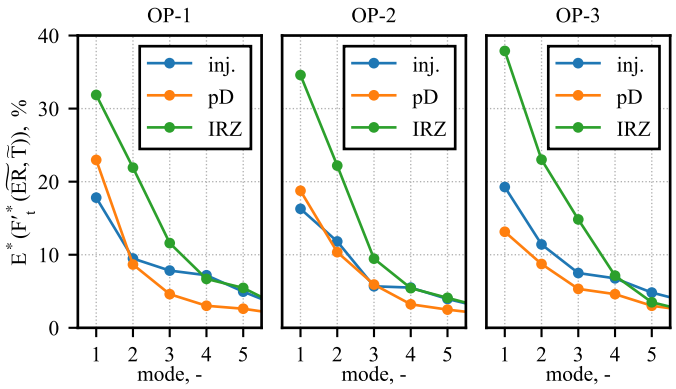

Figure 18: Energy content of $F_t'^*(\widetilde{ER}\text{-}\widetilde{T})$ LFD modes computed in sampling volumes near the injector (inj.), at the peripheryDown location (pD) and in the inner recirculation zone (IRZ). Lines serve as a guidance for the eye.

Figure 19 compares the spatial modes $\phi_{1,LFD}(F_t'^*(\widetilde{ER}\text{-}\widetilde{T}))$ of the OPs at the previously investigated locations. Operating condition differences are reflected by the shape of the modes. While OP-1 and OP-2 modes are quite similar, the OP-2 modes are shifted towards higher $\widetilde{ER}$. A different shape is found for the OP-3 modes which scarcely involve lean events. The most significant influence of the secondary air injection is observed in the IRZ. Here, joint statistics at OP-3 are hardly affected by LFD. Recirculation of lean- and rich-burned pockets has been observed at OP-1 experimentally [5, 14]. The first mode reflects this behavior by shifting the frequency between leaner and richer events. In OP-2, deviations from equilibrium in both rich and lean direction are caused by this mode. None of the investigated modes in the IRZ affects the probability of events in soot formation promoting conditions ($\widetilde{ER} > 1.7$). Modes at the peripheryDown location and near the injector are similar at each OP, respectively. The affected $\widetilde{ER}$ range at pD is slightly narrower since the fluid mixture is approaching equilibrium. Close to the injector, modes at all OPs affect the probability of soot formation promoting events in the same way: Negative temporal mode coefficients rise the probability of these events. At pD this is observed for OP-2 only. In conclusion, a high energy mode is found near the injector at all OPs that similarly affects the probability of soot formation promoting events.

Figure 20 shows the cross-correlation of the statistic modes with $Z'_{inj.}$, the soot volume and the previously discussed velocity modes (see Fig. 17). The correlation between $a_{1,LFD}(Z'_{inj.})$ and

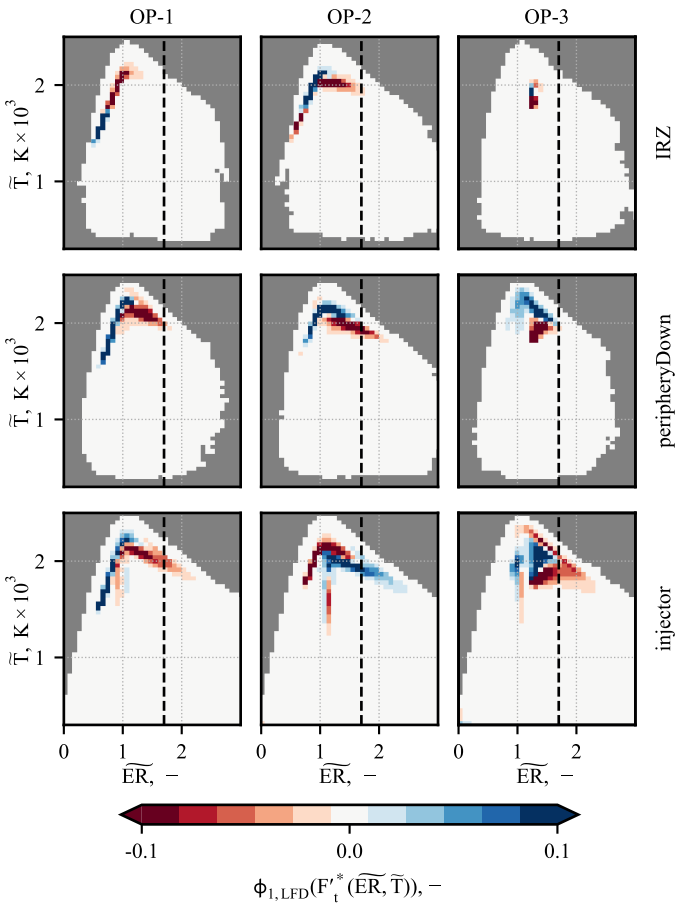

Figure 19: First spatial mode of LFD bandpass filtered temperature equivalence ratio statistics $F_t'^*(\widetilde{ER}\text{-}\widetilde{T})$ sampled at different locations for all operating conditions. **- - -** $\widetilde{ER} = 1.7$.

$a_{1,LFD}(F_t'^*(\widetilde{ER}\text{-}\widetilde{T})_{inj.})$ is significant for all OPs which means that both modes describe the same phenomenon. Consequentially, the correlation between $a_{1,LFD}(F_t'^*(\widetilde{ER}\text{-}\widetilde{T})_{inj.})$ and $\iiint \widetilde{f}_v dV$ are significant as well while the other $F_t'^*(\widetilde{ER}\text{-}\widetilde{T})_{inj.}$ LFD modes are much less correlated with the soot volume in the combustor. Since $a_{1,LFD}(F_t'^*(\widetilde{ER}\text{-}\widetilde{T})_{inj.})$ contains much more energy and is a more general variable as the mixture fraction, its correlations are slightly weaker than for $a_{1,LFD}(Z'_{inj.})$ and $\iiint \widetilde{f}_v dV$ (see Fig. 17). The correlation with the velocity modes leads to the same conclusion as for $a_{1,LFD}(Z'_{inj.})$: The correlation between the joint statistics mode and axially symmetric velocity modes is best.

In summary, mode analysis of joint statistics proofed valuable. The mode analysis of $\widetilde{ER}\text{-}\widetilde{T}$ statistics confirms the findings of the $a_{1,LFD}(Z'_{inj.})$ based mode analysis. This agreement gives confidence in the conclusion that the low frequency flow field and soot dynamics are linked via the mixture fraction close to the injector and that this process is similar at all OPs.

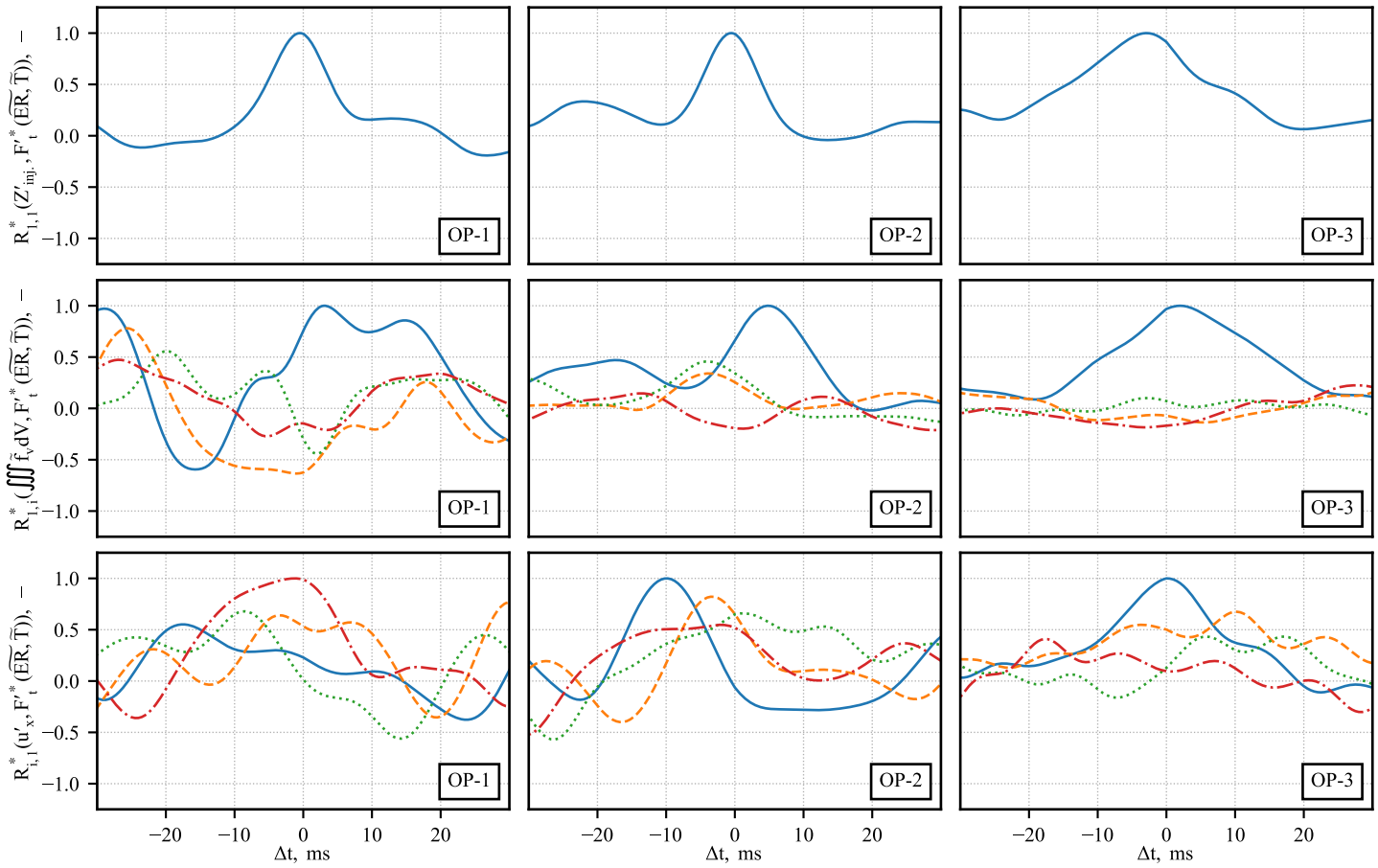

Figure 20: Normalized cross-correlation of LFD modes of temperature equivalence ratio statistics with mixture fraction (top), soot volume (middle) and velocity (bottom) for reacting conditions. $i = 1$, $i = 2$, $i = 3$, $i = 4$.

7. Conclusion

Soot formation in the aero-engine model combustor is highly intermittent. The present work enhances the knowledge on how the flow field dynamics influence soot formation. This is achieved by statistical and modal analysis at three operating points which are chosen to investigate the effect of secondary air injection and primary equivalence ratio. Finite-rate chemistry based LES, combined with a well validated sectional soot model, provides the data for the investigation. Simulation results are verified by a thorough validation and a statistical analysis. This procedure ensures, that the subsequent mode analysis only includes well predicted soot evolution phenomena. Even though soot decrease is overestimated in the downstream part of the combustor, the soot formation close to the injector is predicted well by the LES. Hence, the operating condition influence on soot formation is investigated.

Multiresolution POD enabled a frequency-based separation of coherent and incoherent modes to analyze their impact on soot. MRPOD revealed, that the PVC and low frequency dynamics are the dominant flow field dynamics at all OPs. While soot precursors are only weakly affected by LFD due to the nonlinear soot chemistry, the LFD influence on soot is stronger at all OPs.

An equivalence ratio mode reconstruction proofed, that at OP-1 and OP-3 the PVC is crucial to provide sufficiently rich conditions to enable soot formation. Moreover, the PVC has a local impact on soot precursors and soot as shown by the phase shift of their reconstructed modes. Both depend on PVC induced mixing and the resulting chemical reactions in the IRZ close to the primary injector. Outside of the IRZ, the present analysis indicates that PVC just transports chemical species. Secondary air injection and primary equivalence ratio do not influence this behavior at the conditions investigated.

A thorough low frequency dynamics analysis has been performed for the mixture fraction field and joint equivalence ratio temperature statistics. It appears as an axially symmetric mode in mixture fraction field and as a high energetic mode in $\widetilde{ER}$-$\widetilde{T}$ statistics which affects the probability of fuel-rich events that support soot formation. This mode correlates well with an axially symmetric velocity mode near the primary injector that is found in the case without secondary air injection. Secondary air injection causes LFD velocity modes with much more energy which involve also the recirculation zone and the secondary air injection jets. Comparison with non-reacting conditions suggests, that an axially symmetric mode is present as well which gets distributed in the incoherent LFD modes. These highly intermittent modes and the leaner recirculated gas cause a higher

intermittence of soot formation by oxidation air influence. An increased primary equivalence ratio decreases the intermittence since operating conditions are shifted away from the sooting limit.

It may be summarized that:

- The strong dependence of soot formation on the PVC and LFD dynamics makes their correct prediction essential for soot simulations of swirl combustors.
- Magnitude of soot intermittence can be reduced by an increased primary equivalence ratio.
- Secondary air injection increases the intermittence due to lean gas recirculation.

In conclusion, a methodological procedure to quantitatively analyze the cause of the soot intermittence in an aero-engine model-combustor is presented. Evidence is provided, that the intermittence at all OPs is linked to axially symmetric low frequency dynamics in the velocity field which affect the equivalence ratio near the primary injector. Subsequent nonlinear response of soot chemistry is intensified by the operating conditions which are close to the sooting limit. A strong soot formation intermittence is the result.

Acknowledgements

The authors thank F. Eigentler, Dr. A. Fiolitakis, Dr. K. P. Geigle and Dr. Z. Yin for their contribution to this work. Funding from the European Union within the project SOPRANO (Soot Processes and Radiation in Aeronautical innovative combustion) Horizon 2020 Grant Agreement No. 690724 is gratefully acknowledged. The authors gratefully acknowledge the Gauss Centre for Supercomputing e.V. (www.gauss-centre.eu) for funding this project by providing computing time through the John von Neumann Institute for Computing (NIC) on the GCS Supercomputer JUWELS [78] at Jülich Supercomputing Centre (JSC).

References

[1] I. M. Kennedy, The health effects of combustion-generated aerosols, Proc. Combust. Inst. 31 (2007) 2757 – 2770.

[2] U. Burkhardt, L. Bock, A. Bier, Mitigating the contrail cirrus climate impact by reducing aircraft soot number emissions, npj Clim. Atmos. Sci. 1 (2018).

[3] D. S. Lee, D. W. Fahey, A. Skowron, M. R. Allen, U. Burkhardt, Q. Chen, S. J. Doherty, S. Freeman, P. M. Forster, J. Fuglestvedt, A. Gettelman, R. R. D. León, L. L. Lim, M. T. Lund, R. J. Millar, B. Owen, J. E. Penner, G. Pitari, M. J. Prather, R. Sausen, L. J. Wilcox, The contribution of global aviation to anthropogenic climate forcing for 2000 to 2018, Atmos. Environ. 244 (2021) 117834.

[4] K. P. Geigle, R. Hadef, W. Meier, Soot formation and flame characterization of an aero-engine model combustor burning ethylene at elevated pressure, J. Eng. Gas Turbines Power 136 (2014) 021505.

[5] M. Stöhr, K. Geigle, R. Hadef, I. Boxx, C. Carter, M. Grader, P. Gerlinger, Time-resolved study of transient soot formation in an aero-engine model combustor at elevated pressure, Proc. Combust. Inst. 37 (2019) 5421–5428.

[6] S. T. Chong, V. Raman, M. E. Mueller, H. G. Im, The role of recirculation zones in soot formation in aircraft combustors, Proceedings of ASME Turbo Expo (2018) GT2018–76217.

[7] M. Grader, Z. Yin, K. P. Geigle, P. Gerlinger, Influence of flow field dynamics on soot evolution in an aero-engine model combustor, Proc. Combust. Inst. 38 (2021) 6421–6429.

[8] C. Eberle, P. Gerlinger, K. P. Geigle, M. Aigner, Numerical investigation of transient soot evolution processes in an aero-engine model combustor, Combust. Sci. Technol. 187 (2015) 1841–1866.

[9] K. P. Geigle, M. Köhler, W. O'Loughlin, W. Meier, Investigation of soot formation in pressurized swirl flames by laser measurements of temperature, flame structures and soot concentrations, Proc. Combust. Inst. 35 (2015) 3373 – 3380.

[10] S. T. Chong, M. Hassanaly, H. Koo, M. E. Mueller, V. Raman, K.-P. Geigle, Large eddy simulation of pressure and dilution-jet effects on soot formation in a model aircraft swirl combustor, Combust. Flame 192 (2018) 452–472.

[11] K. P. Geigle, W. O'Loughlin, R. Hadef, W. Meier, Visualization of soot inception in turbulent pressurized flames by simultaneous measurement of laser-induced fluorescence of polycyclic aromatic hydrocarbons and laser-induced incandescence, and correlation to oh distributions, Appl. Phys. B 119 (2015) 717–730.

[12] K. P. Geigle, R. Hadef, M. Stöhr, W. Meier, Flow field characterization of pressurized sooting swirl flames and relation to soot distributions, Proc. Combust. Inst. 36 (2017) 3917 – 3924.

[13] P. Nau, Z. Yin, K. P. Geigle, W. Meier, Wall temperature measurements at elevated pressures and high temperatures in sooting flames in a gas turbine model combustor, Appl. Phys. B 123 (2017) 279.

[14] I. Litvinov, J. Yoon, C. Noren, M. Stöhr, I. Boxx, K. P. Geigle, Time-resolved study of mixing and reaction in an aero-engine model combustor at increased pressure, Combust. Flame 231 (2021) 111474.

[15] International Sooting Flame (ISF) Workshop website. URL: `https://www.adelaide.edu.au/cet/isfworkshop/data-sets/`, accessed 01/08/2021.

[16] A. Wick, F. Priesack, H. Pitsch, Large-eddy simulation and detailed modeling of soot evolution in a model aero engine combustor, Proceedings of ASME Turbo Expo (2017) GT2017–63293.

[17] S. T. Chong, V. Raman, M. E. Mueller, P. Selvaraj, H. G. Im, Effect of soot model, moment method, and chemical kinetics on soot formation in a model aircraft combustor, Proc. Combust. Inst. 37 (2019) 1065–1074.

[18] F. Dupoirieux, N. Bertier, C. Guin, L.-H. Dorey, K. P. Geigle, C. Eberle, P. Gerlinger, Methodology for the numerical prediction of pollutant formation in gas turbine combustors and associated validation experiments, AerospaceLab J. 2 (2016) 15–33.

[19] B. Franzelli, E. Riber, B. Cuenot, M. Ihme, Numerical modeling of soot production in aero-engine combustors using large eddy simulations, Proceedings of ASME Turbo Expo (2015) GT2015–43630.

[20] A. Felden, E. Riber, B. Cuenot, Impact of direct integration of analytically reduced chemistry in LES of a sooting swirled non-premixed combustor, Combust. Flame 191 (2018) 270–286.

[21] L. Gallen, A. Felden, E. Riber, B. Cuenot, Lagrangian tracking of soot particles in LES of gas turbines, Proc. Combust. Inst. 37 (2019) 5429–5436.

[22] P. Rodrigues, O. Gicquel, N. Darabiha, K. P. Geigle, R. Vicquelin, Assessment of external heat transfer modeling of a laboratory-scale combustor: Effects of pressure-housing environment and semi-transparent viewing windows, J. Eng. Gas Turbines Power 141 (2018).

[23] L. Tardelli, B. Franzelli, P. Rodrigues, N. Darabiha, Impact of the reaction mechanism model on soot growth and oxidation in laminar and turbulent flames, Proceedings of ASME Turbo Expo (2019) GT2019–90873.

[24] S. Paccati, D. Bertini, L. Mazzei, S. Puggelli, A. Andreini, Large-eddy simulation of a model aero-engine sooting flame with a multiphysics approach, Flow Turbul. Combust. 106 (2020) 1329–1354.

[25] M. Grader, C. Eberle, P. Gerlinger, M. Aigner, LES of a pressurized, sooting aero-engine model combustor at different equivalence ratios with a sectional approach for PAHs and soot, Proceedings of ASME Turbo Expo (2018) GT2018–75254.

[26] C. Eberle, P. Gerlinger, K. P. Geigle, M. Aigner, Toward finite-rate chemistry large-eddy simulations of sooting swirl flames, Combust. Sci. Technol. 190 (2018) 1194–1217.

[27] B. Franzelli, A. Vié, N. Darabiha, A three-equation model for the prediction of soot emissions in LES of gas turbines, Proc. Combust. Inst. 37 (2019) 5411–5419.

[28] H. Koo, V. Raman, M. E. Mueller, K.-P. Geigle, LES of a sooting flame in a pressurized swirl combustor, Proc. 54th AIAA Aerospace Sciences Meeting (2016) AIAA 2016–2123.

[29] C. Eberle, P. Gerlinger, M. Aigner, A sectional PAH model with reversible PAH chemistry for CFD soot simulations, Combust. Flame 179 (2017) 63–73.

[30] C. Eberle, P. M. Gerlinger, M. Aigner, Large-eddy simulations of a sooting lifted turbulent jet-flame, Proc. 55th AIAA Aerospace Sciences Meeting (2017) AIAA 2017–1785.

[31] M. Grader, C. Eberle, P. Gerlinger, Large-eddy simulation and analysis of a sooting lifted turbulent jet flame, Combust. Flame 215 (2020) 458–470.

[32] D. Gu, Z. Sun, B. B. Dally, P. R. Medwell, Z. T. Alwahabi, G. J. Nathan, Simultaneous measurements of gas temperature, soot volume fraction and primary particle diameter in a sooting lifted turbulent ethylene/air non-premixed flame, Combust. Flame 179 (2017) 33–50.

[33] V. Narayanaswamy, N. Clemens, Simultaneous LII and PIV measurements in the soot formation region of turbulent non-premixed jet flames, Proc. Combust. Inst. 34 (2013) 1455–1463.

[34] P. Donde, V. Raman, M. E. Mueller, H. Pitsch, Les/pdf based modeling of soot–turbulence interactions in turbulent flames, Proc. Combust. Inst. 34 (2013) 1183 – 1192.

[35] K. Taira, S. L. Brunton, S. T. M. Dawson, C. W. Rowley, T. Colonius, B. J. McKeon, O. T. Schmidt, S. Gordeyev, V. Theofilis, L. S. Ukeiley, Modal analysis of fluid flows: An overview, AIAA J. 55 (2017) 4013–4041.

[36] P. J. Schmid, Dynamic mode decomposition of numerical and experimental data, J. Fluid Mech. 656 (2010) 5–28.

[37] Z. Yin, M. Stöhr, Time–frequency localisation of intermittent dynamics in a bistable turbulent swirl flame, J. Fluid Mech. 882 (2020) A30.

[38] M. Sieber, C. O. Paschereit, K. Oberleithner, Spectral proper orthogonal decomposition, J. Fluid Mech. 792 (2016) 798–828.

[39] M. A. Mendez, M. Balabane, J.-M. Buchlin, Multi-scale proper orthogonal decomposition of complex fluid flows, J. Fluid Mech. 870 (2018) 988–1036.

[40] E. Kaiser, B. R. Noack, L. Cordier, A. Spohn, M. Segond, M. Abel, G. Daviller, J. Östh, S. Krajnović, R. K. Niven, et al., Cluster-based reduced-order modelling of a mixing layer, J. Fluid Mech. 754 (2014) 365–414.

[41] S. Barwey, M. Hassanaly, Q. An, V. Raman, A. Steinberg, Experimental data-based reduced-order model for analysis and prediction of flame transition in gas turbine combustors, Combust. Theory Model. 23 (2019) 994–1020.

[42] S. L. Brunton, B. R. Noack, P. Koumoutsakos, Machine learning for fluid mechanics, Annu. Rev. Fluid Mech. 52 (2020) 477–508.

[43] K. Taira, M. S. Hemati, S. L. Brunton, Y. Sun, K. Duraisamy, S. Bagheri, S. T. M. Dawson, C.-A. Yeh, Modal analysis of fluid flows: Applications and outlook, AIAA J. 58 (2020) 998–1022.

[44] A. Kronenburg, R. Bilger, J. Kent, Modeling soot formation in turbulent methane–air jet diffusion flames, Combust. Flame 121 (2000) 24–40.

[45] A. Attili, F. Bisetti, M. E. Mueller, H. Pitsch, Formation, growth, and transport of soot in a three-dimensional turbulent non-premixed jet flame, Combust. Flame 161 (2014) 1849–1865.

[46] L. Tian, M. A. Schiener, R. P. Lindstedt, Fully coupled sectional modelling of soot particle dynamics in a turbulent diffusion flame, Proc. Combust. Inst. 38 (2021) 1365–1373.

[47] F. Bisetti, G. Blanquart, M. E. Mueller, H. Pitsch, On the formation and early evolution of soot in turbulent nonpremixed flames, Combust. Flame 159 (2012) 317–335.

[48] D. O. Lignell, J. H. Chen, P. J. Smith, Three-dimensional direct numerical simulation of soot formation and transport in a temporally evolving nonpremixed ethylene jet flame, Combust. Flame 155 (2008) 316–333.

[49] S. S. Girimaji, Assumed β-pdf model for turbulent mixing: Validation and extension to multiple scalar mixing, Combust. Sci. Technol. 78 (1991) 177–196.

[50] P. Gerlinger, Investigation of an assumed pdf approach for finite-rate chemistry, Combust. Sci. Technol. 175 (2003) 841–872.

[51] J. Bardina, J. Ferziger, W. Reynolds, Improved subgrid-scale models for large-eddy simulation, Proc. 13th Fluid and Plasma Dynamics Conference (1980) AIAA 1980–1357.

[52] A. W. Cook, J. J. Riley, A subgrid model for equilibrium chemistry in turbulent flows, Phys. Fluids 6 (1994) 2868–2870.

[53] H. Wang, N. Qin, M. Sun, H. Wu, Z. Wang, A hybrid LES (large eddy simulation)/assumed sub-grid PDF (probability density function) model for supersonic turbulent combustion, Sci. China Technol. Sci. 54 (2011) 2694.

[54] A. Kempf, R. P. Lindstedt, J. Janicka, Large-eddy simulation of a bluff-body stabilized non-premixed flame, Combust. Flame 144 (2006) 170–189.

[55] P. Gerlinger, B. Noll, M. Aigner, Assumed pdf modelling and pdf structure investigation using finite-rate chemistry, Prog. Comput. Fluid Dyn., Int. J. 5 (2005) 334–344.

[56] M. E. Mueller, H. Pitsch, Large eddy simulation subfilter modeling of soot-turbulence interactions, Phys. Fluids 23 (2011) 115104.

[57] F. Nicoud, F. Ducros, Subgrid-scale stress modelling based on the square of the velocity gradient tensor, Flow Turbul. Combust. 62 (1999) 183–200.

[58] H. A. Michelsen, M. B. Colket, P.-E. Bengtsson, A. D'Anna, P. Desgroux, B. S. Haynes, J. H. Miller, G. J. Nathan, H. Pitsch, H. Wang, A review of terminology used to describe soot formation and evolution under combustion and pyrolytic conditions, ACS Nano 14 (2020) 12470–12490.

[59] N. Slavinskaya, P. Frank, A modelling study of aromatic soot precursors formation in laminar methane and ethene flames, Combust. Flame 156 (2009) 1705 – 1722.

[60] N. Slavinskaya, O. Haidn, Reduced chemical model for high pressure methane combustion with PAH formation, Proc. 46th AIAA Aerospace Sciences Meeting and Exhibit (2008) AIAA 2008–1012.

[61] T. Blacha, M. Di Domenico, P. Gerlinger, M. Aigner, Soot predictions in premixed and non-premixed laminar flames using a sectional approach for PAHs and soot, Combust. Flame 159 (2012) 181–193.

[62] M. Köhler, K.-P. Geigle, T. Blacha, P. Gerlinger, W. Meier, Experimental characterization and numerical simulation of a sooting lifted turbulent jet diffusion flame, Combust. Flame 159 (2012) 2620–2635.

[63] N. Dellinger, N. Bertier, F. Dupoirieux, G. Legros, Hybrid eulerian-lagrangian method for soot modelling applied to ethylene-air premixed flames, E. 194 (2020) 116858.

[64] M. di Domenico, P. Gerlinger, M. Aigner, Development and validation of a new soot formation model for gas turbine combustor simulations, Combust. Flame 157 (2010) 246–258.

[65] M. Frenklach, H. Wang, Detailed mechanism and modeling of soot particle formation, in: H. Bockhorn (Ed.), Soot Formation in Combustion, Springer Berlin Heidelberg, 1994, pp. 165–192.

[66] H. Richter, S. Granata, W. H. Green, J. B. Howard, Detailed modeling of pah and soot formation in a laminar premixed benzene/oxygen/argon low-pressure flame, Proc. Combust. Inst. 30 (2005) 1397 – 1405.

[67] C. J. Pope, J. B. Howard, Simultaneous particle and molecule modeling (SPAMM): An approach for combining sectional aerosol equations and elementary gas-phase reactions, Aerosol Sci. Technol. 27 (1997) 73–94.

[68] F. Setzwein, P. Ess, P. Gerlinger, An implicit high-order k-exact finite-volume approach on vertex-centered unstructured grids for incompressible flows, J. Comput. Phys. 446 (2021) 110629.

[69] A. J. Chorin, Numerical solution of the navier-stokes equations, Math. Comput. 22 (1968) 745–745.

[70] L. Sirovich, Turbulence and the dynamics of coherent structures. i. coherent structures, Q. Appl. Math. 45 (1987) 561–571.

[71] I. Daubechies, Ten Lectures on Wavelets, Society for Industrial and Applied Mathematics, 1992.

[72] P. Rodrigues, Modélisation multiphysique de flammes turbulentes suitées avec la prise en compte des transferts radiatifs et des transferts de chaleur pariétaux, Ph.D. thesis, Université Paris-Saclay, 2018.

[73] B. Franzelli, L. Tardelli, M. Stöhr, K. Geigle, P. Domingo, Assessment of les of intermittent soot production in an aero-engine model combustor using high-speed measurements, Proc. Combust. Inst. (2022) In Press.

[74] C. Gu, H. Lin, J. Camacho, B. Lin, C. Shao, R. Li, H. Gu, B. Guan, Z. Huang, H. Wang, Particle size distribution of nascent soot in lightly and heavily sooting premixed ethylene flames, Combust. Flame 165 (2016) 177–187.

[75] M. Stöhr, R. Sadanandan, W. Meier, Phase-resolved characterization of vortex–flame interaction in a turbulent swirl flame, Exp. Fluids 51 (2011) 1153–1167.

[76] M. Stöhr, C. Arndt, W. Meier, Transient effects of fuel-air mixing in a partially-premixed turbulent swirl flame, Proc. Combust. Inst. 35 (2015) 3327 – 3335.

[77] M. Stöhr, K. Oberleithner, M. Sieber, Z. Yin, W. Meier, Experimental study of transient mechanisms of bistable flame shape transitions in a swirl combustor, J. Eng. Gas Turbines Power 140 (2017) 011503.

[78] Jülich Supercomputing Centre, JUWELS: Modular Tier-0/1 Supercomputer at the Jülich Supercomputing Centre, J. large-scale res. facilit. 5 (2019) A135.